FINITE ELEMENT STUDY OF PLANE WAVE ACOUSTIC PHENOMENA IN DUCTS

Juan Fernando Betts

Thesis submitted to the Faculty of the

Virginia Polytechnic Institute and State University

in partial fulfillment of the requirements for the degree of

MASTER OF SCIENCE

in

Mechanical Engineering

C.E. Knight, Chairman

R. Burdisso

R. West

April 29, 1998

Blacksburg, Virginia

Key Words: Finite Elements, Acoustics, Waves, Ducts

FINITE ELEMENT STUDY OF PLANE WAVE ACOUSTIC PHENOMENA IN DUCTS

This thesis studied the finite element modeling of plane wave acoustic phenomena in ducts. The study looked into finite element factors such as shape functions, mesh refinement, and element distortion.

The study concluded that the higher order shape function eight-node quadrilateral element gave considerably better results than lower order shape function four-node quadrilateral element. The eight-node element converged much faster to the analytical solution than the four-node element. The average error, taking all the cases in consideration, for the four-node element was around 30 % for a mesh refinement of about 14 elements per wavelength at 100 Hz frequency. The eight-node element in the other hand had average absolute errors of less than 1% under the same conditions.

This section also found that the eight-node element was substantially more resistant to solution deterioration due to element distortion than the four-node element. For example distorting the four-node element up to 60° degrees usually increased errors very rapidly to above 100 % errors. The eight-node element on the other hand usually produced errors of less than 5 % for the same level of distortion.

The study showed that the type of boundary condition used had a significant effect on the solution accuracy. The study demonstrated that the effect of the natural boundary conditions was more global. Meeting this kind of boundary condition through mesh convergence produced accurate results throughout the duct.

To My Parents

Acknowledgements

I would like to thank my advisor Dr. Charles Knight for invaluable advice in guiding this research. I would also like to thank him for his patience and time in correcting and re-correcting this thesis to give it the proper professional form and for teaching me much of what I know about finite elements.

I would also like to thank Dr. Ricardo Burdisso for his time and advice in criticizing this research work and challenging me to understand the principles being studied. I would also like to thank him for taking the time to go over the analytical section of this thesis and for teaching me much of what I know of acoustics.

Moreover I would like to thank Dr. Robert West for taking the time to review this thesis. Finally I would like to thank all the people that helped me in accomplishing this research. Lori Brady for helping me with SYSNOISE Finite Element and Boundary Element Software. Felix Nevarez and Mary Kafura for their help with UNIX and in how to accommodate the hundreds of result files created for this thesis.

Table of Content

Chapter 1

Introduction

1.1 Purpose and Methods

The finite element method is an approximate numerical techniques used to solve a given governing partial differential equation of a system. This study arises out of the need to determine the modeling factors and practices that lead to good reliable finite element results in acoustics.

The need for reliable results is complicated because the results' accuracy depend on the problem being modeled. Nevertheless, by looking at factors that affect the solution of the finite element method, good modeling practices can be established that are likely to lead to reliable results.

The problem modeled in this study was that of plane acoustic waves traveling in a duct created by a harmonic exciting pressure field. The plane wave phenomena was a good choice, because this system is easy to understand, and most readers would readily understand the physics of this system. Further, the analytical solution for this problem was easily attainable in closed form, which allowed easy comparison to finite element solutions.

The finite element method was analyzed in terms of the following factors:

- Mesh Refinement
- Element Distortion
- Order of the Interpolation Functions
- Boundary Condition Type

The geometry used in the finite element method was a duct 20 meters long and 3 meters high as illustrated in Fig. 1. Several cases were analyzed under different boundary condition sets on each of the faces. This was done to determine the overall modeling characteristics of the finite element method for several solution fields.

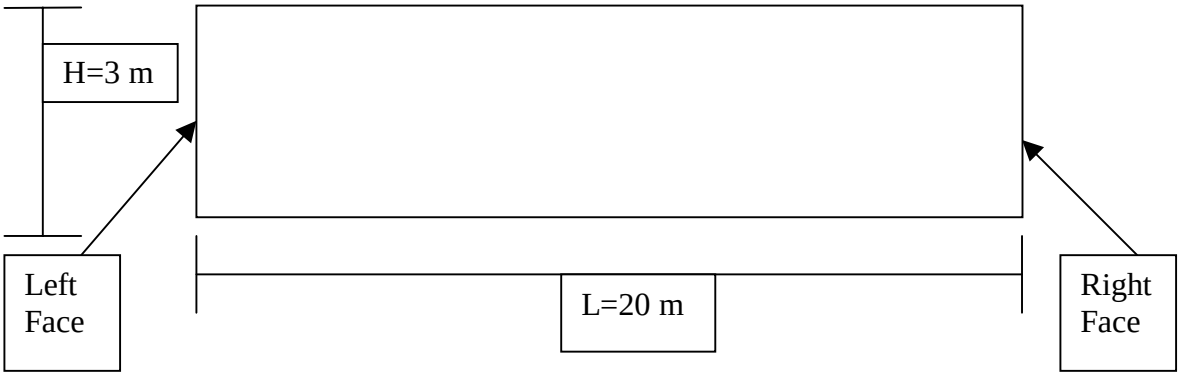

Figure 1. Geometry modeled.

1.2 Literature Review

There are other numerical studies available in the literature that deal with similar acoustic problems [1-4]. Some of the older studies like that by I. Tag and E. Lumsdaine [1] dealt with the non-linear three-dimensional acoustic equation in axisymmetric ducts. This study was mainly concerned with high subsonic Mach numbers and comparison of the results with experimental solutions. The authors of this study were concerned with meeting the experimental solution, yet no mention was made of the modeling practices used to obtain reliable results.

Another early study by R.J. Astley and W. Eversman [2] looked at comparison of the finite element method and the method of weighted residuals. The authors of this study gave some insight into the modeling practices used to obtain their results. The authors looked at mesh refinement to predict transmission and reflection coefficients. Although more complete, in terms of giving insight into the modeling practices, than Lumsdaine's study, many more modeling factors are presented in this study.

More recent studies by I. Danda Roy and W. Eversman [3] have improved solutions over these earlier studies. In their study for example an eigen-value acoustic duct problem was solved with the finite element method. Improved solutions were obtained by evaluating the acoustic pressure at gauss points rather than nodal points.

Although solution improvement was shown by their study by evaluating the acoustic pressure at gauss points there are many more modeling factors in the finite

element method that affect the solution accuracy. The authors of this study stated that 4 to 5 elements per wavelength in the direction of the sound propagation would produce “good” results.

There are more of these kinds of finite element studies documented in the literature. Most of them were trying to achieve good results without necessarily explaining the modeling practices that led to them [4-5].

This thesis intends to study some factors that affect the finite element solution in duct acoustics. It does not encompasses all possible acoustic problems, therefore extrapolation of the results of this study to other problems should be done with care. It is preferable that the readers understand the physics and numerical methods and weight the factors affecting the solution accuracy to each situation.

Chapter 2

Theoretical Analysis

2.1 Fundamentals of Acoustics

The most important equation in acoustics is the acoustic wave equation also known as the Helmholtz's equation. To derive the Helmholtz's equation we must first examine three other equations.

The first of these equations is the equation of state. This equation relates the internal forces of the fluid to the deformation of the fluid. The second equation is the equation of continuity. This equation considers the conservation of mass for the fluid. The final equation is Euler's equation, which is analogous to Newton's momentum equation in solids [6].

A. Equation of State

Let's assume we have a volume of fluid with density ρ_o and pressure $\mathbf{P_o}$. When this volume is deformed the density and the pressure change to ρ and **P** respectively as can be seen in Fig. 2.

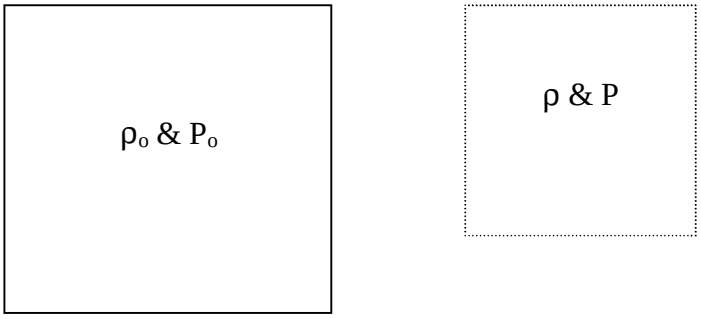

Figure 2. Volume of Fluid.

The new pressure in the fluid using Taylor series expansion is given by

$$P = P_o + \frac{\partial P}{\partial \rho} d\rho \tag{1}$$

Approximating equation (1) assuming small deformations leads to

$$P \approx P_o + \frac{\partial P}{\partial \rho}(\rho - \rho_o) \tag{2}$$

The Bulk modulus of a fluid is defined as

$$B = \rho_o \frac{\partial P}{\partial \rho} \tag{3}$$

Rearranging produces

$$\frac{B}{\rho_0} = \frac{\partial P}{\partial \rho} \tag{4}$$

Inserting equation (4) into equation (3) and rearranging leads to

$$P - P_o = B\frac{\rho - \rho_o}{\rho_o} \tag{5}$$

If **p,** the acoustic pressure, and **s,** the condensation of the fluid, are defined as

$$p = P - P_o \tag{6}$$

$$s = \frac{\rho - \rho_o}{\rho_o} \tag{7}$$

Equation (5) becomes

$$p = Bs \tag{8}$$

Equation (8) is the equation of state.

B. Equation of Continuity

Figure 3 shows fluid entering and leaving a differential volume. The symbol $\mathbf{u_x}$ stands for the fluid velocity. To get the continuity equation we need to assume that the change in the amount of fluid entering and leaving a differential volume is equal to the amount of fluid increase inside the volume.

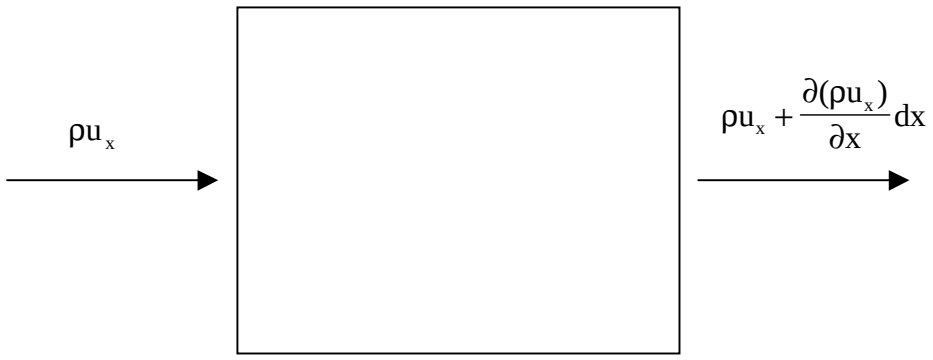

Figure 3. Fluid volume with fluid coming in on the left and leaving on the right.

This yields for one-dimensional flow to

$$\{\rho u_x - [\rho u_x + \frac{\partial(\rho u_x)}{\partial x} dx]\} dydz = -\frac{\partial(\rho u_x)}{\partial x} dxdydz = \frac{\partial \rho}{\partial t} dxdydz \tag{9}$$

Doing a similar derivation for all three spatial directions and letting **dV=dxdydz** produces

$$-[\frac{\partial \rho u_x}{\partial x} + \frac{\partial \rho u_y}{\partial y} + \frac{\partial \rho u_z}{\partial z}] dV = \frac{\partial \rho}{\partial t} dV \tag{10}$$

Equation (10) in compacted notation is

$$-[\nabla \bullet (\rho \vec{u})] = \frac{\partial \rho}{\partial t} \tag{11}$$

Rearranging equation (11) produces

$$\frac{\partial \rho}{\partial t} + [\nabla \bullet (\rho \vec{u})] = 0 \tag{12}$$

Equation (12) is a nonlinear partial differential equation. Both **u** and **ρ** are functions of space and time. Equation (12) needs to be linearized. To do this the chain rule for a divergence operator needs to be employed in order to change equation (12) to the proper form. The chain rule for a divergence operator is

$$\nabla \bullet (u\vec{A}) = (\nabla u) \bullet \vec{A} + u(\nabla \bullet \vec{A}) \tag{13}$$

where **u** is a scalar and **A** is a vector in equation (13). Using the relationship in equation (13) in equation (12) yields

$$\frac{\partial \rho}{\partial t} + (\nabla \rho) \bullet \vec{u} + \rho(\nabla \bullet \vec{u}) = 0 \tag{14}$$

Replacing **ρ** with **ρ_o(1+s)** in equation (14), where **ρ_o** is the original density (a constant) and **s** is the condensation of the fluid produces

$$\rho_o \frac{\partial s}{\partial t} + (\rho_o \nabla s) \bullet \vec{u} + (\rho_o + \rho_o s)(\nabla \bullet \vec{u}) = 0 \tag{15}$$

Simplifying

$$\frac{\partial s}{\partial t} + (\nabla s) \bullet \vec{u} + (1 + s)(\nabla \bullet \vec{u}) = 0 \tag{16}$$

Assuming that $s << 1$ equation (16) becomes

$$\frac{\partial s}{\partial t} + (\nabla \bullet \vec{u}) = 0$$

(17)

Equation (17) is the linearized continuity equation.

C. Euler's Equation

Figure 4 shows pressure forces acting on a fluid element. The net sum of external forces is equal to the mass times the acceleration.

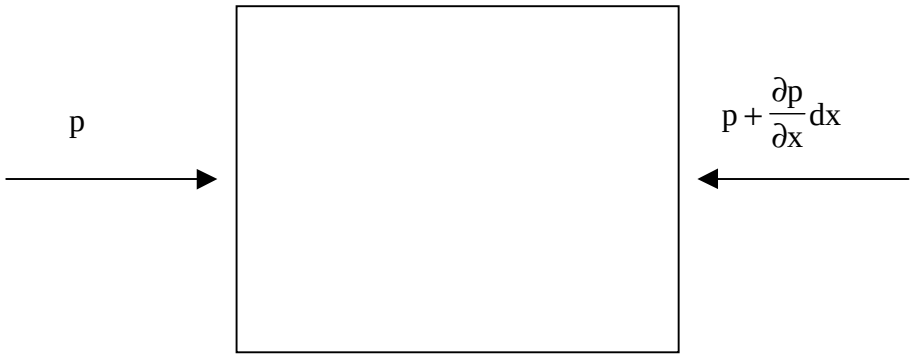

Figure 4. Fluid volume being acted on by pressure forces.

Therefore the sum of the forces in this element in one dimension is

$$p dydz - (p + \frac{\partial p}{\partial x} dx) dydz = \rho \vec{a} dx dydz \tag{18}$$

where **a** is the acceleration of the fluid particles. For all three spatial directions equation (18) becomes

$$-\nabla p = \rho \vec{a} \tag{19}$$

The acceleration for the fluid is given by

$$\vec{a} = \frac{\partial \vec{u}}{\partial t} + u_x \frac{\partial \vec{u}}{\partial x} + u_y \frac{\partial \vec{u}}{\partial y} + u_z \frac{\partial \vec{u}}{\partial z} \tag{20}$$

In compacted notation equation (20) becomes

$$\vec{a} = \frac{\partial \vec{u}}{\partial t} + (\vec{u} \bullet \nabla)\vec{u} \tag{21}$$

Inserting equation (21) into equation (19) results

$$-\nabla p = \rho[\frac{\partial \vec{u}}{\partial t} + (\vec{u} \bullet \nabla)\vec{u}] \tag{22}$$

Assuming that $\partial u/\partial t >> (u \bullet \nabla)u$, then equation (22) becomes

$$-\nabla p = \rho \frac{\partial \vec{u}}{\partial t} \tag{23}$$

Equation (23) is the force equation or Euler's equation.

Now all the elements necessary for deriving the Helmholtz's acoustic equation are present. Taking the divergence of equation (23) and rearranging yields

$$\rho \nabla \bullet \frac{\partial \vec{u}}{\partial t} = -\nabla \bullet (\nabla p) = -\nabla^2 p \tag{24}$$

Next taking the derivative with respect to time of equation (17)

$$\frac{\partial^2 s}{\partial t^2} + \nabla \bullet \frac{\partial \vec{u}}{\partial t} = 0 \tag{25}$$

Combining equations (24) and (25) results in

$$\nabla^2 p = \rho \frac{\partial^2 s}{\partial t^2} \tag{26}$$

Substituting equation (8) into equation (26) yields

$$\nabla^2 p = \frac{1}{c^2} \frac{\partial^2 p}{\partial t^2} \tag{27}$$

where **c** is the phase speed of the fluid. Equation (27) is the pressure wave equation also known as the Helmholtz's equation.

Assuming a harmonic solution, and using equation (23), the fluid velocity is related to the change in the pressure field with respect to space through the following equation

$$v = \frac{-1}{i\omega\rho}\nabla p \tag{28}$$

Where **i** is the imaginary number, and **ω** is the circular frequency.

The relation of the particle velocity to the gradient of the pressure field is called potential flow theory. The equation shows that for a fluid particle to move there has to be a varying pressure field with space. In other words a fluid particle would not move unless there is net pressure acting on it.

The phase speed **c** in Equation (27) is a property of the fluid. It is

$$c = \sqrt{\frac{B}{\rho}} \tag{29}$$

Notice that the phase speed has the same form as the more familiar natural frequency equation for a single degree of freedom in vibration analysis. The equation for a single degree of freedom in vibration analysis is

$$\omega_n = \sqrt{\frac{K}{M}} \tag{30}$$

where **K** and **M** are the stiffness and mass respectively of the vibrational system.

The reason for this similarity is that the phase speed is in actuality the natural frequency for each interacting fluid particle. When a fluid is excited, a wave propagates because each individual fluid particle vibrates at its natural frequency creating a wave that travels at phase speed **c**.

2.2 Analytical Solutions to the Cases in this Study

The study modeled three cases of duct acoustics. Each case had the same geometry as mentioned in the introduction but different boundary conditions. . The boundary conditions for each of the cases was:

- **Case I;** Left Face: Constant Real Pressure Amplitude = 2; Right Face: Impedance = ρc
- **Case II;** Left Face: Constant Real Pressure Amplitude = 2; Right Face: Velocity = 0
- **Case III;** Left Face: Constant Real Pressure Amplitude = 2; Right Face: Pressure = 0

The pressure frequency is held constant at 100 Hz. for all cases in this section. The unit of the pressure amplitude is Pascal. The phase speed **c** and mass density **ρ** are 340 m/s and 1.225 kg/m^3 respectively. The physical significance of these boundary conditions will be explained in chapter 3 (Results & Discussion). Here only the actual algebraic analytical solution of the problem is of interest.

The assumed pressure field solution for the Helmholtz's equation for the cases in this study is

$$p(x,t) = Ae^{i(\omega t - kx)} + Be^{i(\omega t + kx)} \tag{31}$$

where **A** and **B** are arbitrary constants that depend on the boundary conditions of the problem. **ω** is the circular frequency of oscillation, and **k** represents the wave number.

The wave number **k**, is obtained by substituting equation (31) into the Helmholtz's equation (Eqs. 27). Doing so produces

$$k = \frac{\omega}{c} \tag{32}$$

Where **c** is the phase speed given by equation (29). The solution assumed in equation (31) represent two waves traveling in the positive and negative **x** direction.

The boundary condition on the left end is an oscillatory pressure boundary condition $\mathbf{p_o}$ for all cases. Applying this boundary condition to equation (31) results in

$$(A + B)e^{i\omega t} = p_o e^{i\omega t} \tag{33}$$

Simplifying equation (33) yields

$$A + B = p_o \tag{34}$$

Before looking at the other boundary condition in each of the cases, first the general velocity field needs to be derived. Inserting equation (31) into equation (28) produces

$$v(x,t) = \frac{-1}{i\omega\rho}(-ikAe^{-ikx} + ikBe^{ikx})e^{i\omega t} \tag{35}$$

Inserting equation (31) into equation (35) and simplifying leads to

$$v(x,t) = \frac{e^{i\omega t}}{\rho c}(Ae^{-ikx} - Be^{ikx}) \tag{36}$$

The impedance field is the ratio of the pressure field over the velocity field. Therefore the impedance is just equation (31) divided by equation (36). Consequently the impedance field is

$$Z(x) = \rho c\frac{Ae^{-ikx} + Be^{ikx}}{Ae^{-ikx} - Be^{ikx}} \tag{37}$$

where **Z** is the impedance of the fluid. Now all the necessary equations to solve for the pressure and velocity field for the three cases are present.

For case 1 the impedance condition on the right side of the duct is **ρc**. Therefore **Z(L)** is equal to **ρc**, where **L** is equal to the length of the duct. Applying this boundary condition produces

$$\rho c\frac{Ae^{-ikL} + Be^{ikL}}{Ae^{-ikL} - Be^{ikL}} = \rho c \tag{38}$$

Solving simultaneously equation (34) and equation (38) leads to

$$\therefore B = 0 \;\&\; A = p_o \tag{39}$$

Therefore the pressure and velocity fields for Case 1 using equations (31), (36), and (39) produces

$$p(x,t) = p_o e^{-ikx} e^{i\omega t} \tag{40}$$

and

$$v(x,t) = \frac{p_o}{\rho c} e^{-ikx} e^{i\omega t} \tag{41}$$

respectively.

For Case 2 the velocity boundary condition on the right side of the tube is zero. Therefore applying this boundary condition produces

$$\frac{e^{i\omega t}}{\rho c}(Ae^{-ikL} - Be^{ikL}) = 0 \tag{42}$$

Solving simultaneously equation (34) and equation (42) yields

$$A = p_o \frac{e^{ikL}}{2\mathrm{Cos}(kL)} \tag{43}$$

$$B = p_o \frac{e^{-ikL}}{2\mathrm{Cos}(kL)} \tag{44}$$

Consequently the pressure and velocity fields using equations (31), (36), (43) and (44) for Case 2 leads to

$$p(x,t) = \frac{p_o}{2\text{Cos}(kL)}(e^{i(kL-kx)} + e^{-i(kL-kx)})e^{i\omega t} \tag{45}$$

$$v(x,t) = \frac{p_o}{2\rho c\text{Cos}(kL)}(e^{i(kL-kx)} - e^{-i(kL-kx)})e^{i\omega t} \tag{46}$$

Simplifying equations (45) and (46) respectively yields

$$p(x,t) = p_o[\text{Cos}(kx) + \text{Tan}(kL)\text{Sin}(kx)]e^{i\omega t} \tag{47}$$

$$v(x,t) = i\frac{p_o}{\rho c}[\text{Tan}(kL)\text{Cos}(kx) - \text{Sin}(kx)]e^{i\omega t} \tag{48}$$

For Case 3 the pressure boundary condition on the right face of the duct is zero. Applying this boundary condition produces

$$(Ae^{-ikL} + Be^{ikL})e^{i\omega t} = 0 \tag{49}$$

Solving equations (34) and (49) simultaneously leads to

$$A = \frac{p_o e^{ikL}}{i2\text{Sin}(kL)} \tag{50}$$

$$B = p_o[\frac{i2\text{Sin}(kL) - e^{ikL}}{i2\text{Sin}(kL)}] \tag{51}$$

Consequently the pressure and velocity fields for Case 3 using equations (31), (36), (50) and (51) yields

$$p(x,t) = \frac{p_o}{i2Sin(kL)}\{e^{i(kL-kx)} + [i2Sin(kL) - e^{ikL}]e^{ikx}\}e^{i\omega t} \tag{52}$$

$$v(x,t) = \frac{p_o}{i\rho c2Sin(kL)}\{e^{i(kL-kx)} - [i2Sin(kL) - e^{ikL}]e^{ikx}\}e^{i\omega t} \tag{53}$$

Simplifying equation (52) and (53) produces

$$p(x,t) = p_0[Cos(kx) - Cot(kL)Sin(kx)]e^{i\omega t} \tag{54}$$

$$v(x,t) = -i\frac{p_0}{\rho c}[Sin(kx) + Cot(kL)Cos(kx)]e^{i\omega t} \tag{55}$$

These are the analytical solutions of the pressure and velocity fields for all three cases.

2.3 Finite Element Method

The finite element method is a numerical approximation of the solution for a differential equation. In this case, it is an approximation to the Helmholtz equation. Following is the derivation of the finite element method to the Helmholtz equation [7].

The Helmholtz's equation needs to be rearranged so that it equals to zero on the right hand side.

$$\nabla^2 p = \frac{1}{c^2}\frac{\partial^2 p}{\partial t^2} \tag{56}$$

$$\nabla^2 p - \frac{1}{c^2}\frac{\partial^2 p}{\partial t^2} = 0 \tag{57}$$

$$\nabla \bullet (\nabla p) - \frac{1}{c^2}\frac{\partial^2 p}{\partial t^2} = 0 \tag{58}$$

Equation (58) is multiplied by an arbitrary smooth scalar function ϕ and integrated over the domain Ω. The function ϕ satisfies the essential boundary conditions.* Why this is done will become evident later in this derivation.

$$\phi[\nabla \bullet (\nabla p)] - \phi[\frac{1}{c^2}\frac{\partial^2 p}{\partial t^2}] = 0 \tag{59}$$

$$\int_\Omega \phi[\nabla \bullet (\nabla p)]d\Omega - \int_\Omega \phi[\frac{1}{c^2}\frac{\partial^2 p}{\partial t^2}]d\Omega = 0 \tag{60}$$

This is called the **Weak** or **Galerkin's** formulation of the Helmholtz equation.

To transform equation (60) to the proper form, the chain rule of calculus needs to be employed. The chain rule for a gradient operator is

$$\nabla \bullet (u\vec{A}) = (\nabla u) \bullet \vec{A} + u(\nabla \bullet \vec{A}) \tag{61}$$

Rearranging equation (61) produces

$$u(\nabla \bullet \vec{A}) = \nabla \bullet (u\vec{A}) - (\nabla u) \bullet \vec{A} \tag{62}$$

* For a second order differential equation like the Helmholtz's equation, the essential boundary conditions contain no derivatives. Consequently pressure boundary conditions are essential boundary conditions.

Where **u** is a scalar quantity and **A** is a vector. Using the relationship in equation (62) and with **A=∇p** and **u=ϕ** and substituting the result into equation (60) yields

$$\int_{\Omega} \nabla \bullet (\phi \nabla p) d\Omega - \int_{\Omega} \nabla \phi \bullet \nabla p d\Omega - \int_{\Omega} \phi [\frac{1}{c^2} \frac{\partial^2 p}{\partial t^2}] d\Omega = 0 \tag{63}$$

To simplify equation (63) the divergence theorem may be employed. The divergence theorem is

$$\int_{\Omega} \nabla \bullet \vec{A} d\Omega = \int_{\Gamma} \vec{A} \bullet \vec{n} d\Gamma \tag{64}$$

Where **Ω** is still the domain modeled, **Γ** is the boundary of this domain, **A** is an arbitrary vector, and **n** is a unit normal vector to the boundary **Γ**. Using the relationship in equation (64) and applying it to equation (63) produces

$$\int_{\Gamma} \phi \nabla p \bullet \vec{n} d\Gamma - \int_{\Omega} \nabla \phi \bullet \nabla p d\Omega - \int_{\Omega} \phi [\frac{1}{c^2} \frac{\partial^2 p}{\partial t^2}] d\Omega = 0 \tag{65}$$

Simplifying and rearranging

$$\frac{1}{c^2} \int_{\Omega} \phi \frac{\partial^2 p}{\partial t^2} d\Omega + \int_{\Omega} \nabla \phi \bullet \nabla p d\Omega = \int_{\Gamma} \phi \frac{\partial p}{\partial n} d\Gamma \tag{66}$$

The velocity (natural) boundary condition in this problem is given by

$$V_b = \frac{-1}{i\omega\rho} \frac{\partial p}{\partial n} \tag{67}$$

Rearranging equation (67) yields

$$\frac{\partial p}{\partial n} = -i\omega\rho V_b \tag{68}$$

Where the $\mathbf{V_b}$ is the normal boundary velocity, $\boldsymbol{\omega}$ is the circular frequency, and $\boldsymbol{\rho}$ is the density of the fluid. Inserting equation (68) into equation (66) leads to

$$\frac{1}{c^2}\int_{\Omega}\phi\frac{\partial^2 p}{\partial t^2}d\Omega+\int_{\Omega}\nabla\phi\bullet\nabla p d\Omega=-i\omega\rho V_b\int_{\Gamma}\phi d\Gamma \tag{69}$$

Up to equation (69) there has been no approximation to the Helmholtz's equation. If a functional value of **p** could be found that satisfied equation (69) exactly then this functional value of **p** would be the exact solution to this given problem.

Equation (69) requires an approximation since the functional value that exactly satisfies it, is not known. Consequently equation (69) approximated with a finite series sum of nodal values times that node's basis function* produces

$$\phi\approx\phi^n=\phi_i\psi_i(x,y,z)=\phi_i\psi_i \tag{70}$$

$$p\approx p^n=p_j\psi_j(x,y,z)=p_j\psi_j \tag{71}$$

$$\frac{\partial p}{\partial t}\approx\dot{p}^n=\dot{p}_j\psi_j(x,y,z)=\dot{p}_j\psi_j \tag{72}$$

$$\frac{\partial^2 p}{\partial t^2}\approx\ddot{p}^n=\ddot{p}_j\psi_j(x,y,z)=\ddot{p}_j\psi_j \tag{73}$$

where, $\boldsymbol{\psi_i}$ is the basis function for node **i,** $\boldsymbol{\phi_i}$ is the value of the arbitrary function at node **i,** $\mathbf{p_i}$ and its dot derivatives are the pressure values, the derivative with respect to time of the pressure values, and the second derivative of the pressure values with respect to time respectively at node **i**, and the superscript **n** refers to the number of nodes.

Inserting equations (70) through (73) into equation (69) yields

$$\frac{1}{c^2}\int_{\Omega}\phi^n\frac{\partial^2 p^n}{\partial t^2}d\Omega+\int_{\Omega}\nabla\phi^n\bullet\nabla p^n d\Omega=-i\omega\rho V_b\int_{\Gamma}\phi^n d\Gamma \tag{74}$$

$$\frac{\phi_i\ddot{p}_j}{c^2}\int_{\Omega}\psi_i\psi_j d\Omega+\phi_i p_j\int_{\Omega}\nabla\psi_i\bullet\nabla\psi_j d\Omega=-i\phi_i\omega\rho V_b\int_{\Gamma}\psi_i d\Gamma \tag{75}$$

$$[\frac{1}{c^2}\int_{\Omega}\psi_i\psi_j d\Omega]\ddot{p}_j+[\int_{\Omega}\nabla\psi_i\bullet\nabla\psi_j d\Omega]p_j=-i\omega\rho V_b\int_{\Gamma}\psi_i d\Gamma \tag{76}$$

Equation (76) can be simplified by introducing quantities $\mathbf{M_{ij}}$, $\mathbf{K_{ij}}$, and $\mathbf{F_i}$ defined as

$$M_{ij}=\frac{1}{c^2}\int_{\Omega}\psi_i\psi_j d\Omega \tag{77}$$

$$K_{ij}=\int_{\Omega}\nabla\psi_i\bullet\nabla\psi_j d\Omega \tag{78}$$

$$F_i=-i\omega\rho V_b\int_{\Gamma}\psi_i d\Gamma \tag{79}$$

Inserting equations (77) through (79) into equation (76) leads to

$$M_{ij}\ddot{p}_j+K_{ij}p_j=F_i \tag{80}$$

Equation (80) can be rewritten in matrix form as

$$[M]\{\ddot{p}\}+[K]\{p\}=\{F\} \tag{81}$$

The boundary conditions in terms of **p (essential)** are applied to equation (81). These matrix equations are solved simultaneously to get the values of **p** for each node.

In the finite element work the nodes are grouped into elements. Therefore the basis functions are restricted to the elements. This restriction of the basis function to the

---

[*] Basis functions are functions (usually polynomials) whose value is one at its respective node and zero at the remaining nodes [7]. They are defined globally. Throughout this thesis the Einstein summation convention is used. Repeated indices indicate summation over the range of the variable.

element is called shape function. Consequently the element matrices **[M]^e**, **[K]^e**, and **{F}^{e}** are defined as

$$M^e_{ij} = \frac{1}{c^2}\int_{\Omega_e} N_i N_j d\Omega_e \tag{82}$$

$$K^e_{ij} = \int_{\Omega_e} \nabla N_i \bullet \nabla N_j d\Omega_e \tag{83}$$

$$F^e_i = -i\omega\rho V_b \int_{\Gamma_e} N_i d\Gamma_e \tag{84}$$

where $\mathbf{N_i}$, $\mathbf{\Omega_e}$ and $\mathbf{\Gamma_e}$ are the shape function associated with node **i**, the element domain and boundary of the element domain respectively. Since global domain is comprised of the sum of the elements, it follows that the global matrices **[M]**, **[K]**, and **{F}** become the sum of their respective element matrices **[M]^e**, **[K]^e**, and **{F}^{e}**.

The formulator chooses the shape functions and consequently they are an assumed solution field. The shape functions used in this study were the Lagrange shape functions. These are a common set of shape functions, which are polynomials of the lowest possible order for an element type [8]. Consequently each element type has a specific assumed solution field.

The two types of elements used in this study were the four-node and eight-node quadrilateral elements. The assumed pressure fields for a four-node and eight-node quadrilateral element are

$$p(x,y)=\beta_1+ \beta_2 x+ \beta_3 y+ \beta_4 xy \tag{85}$$

$$p(x,y)=\beta_1+ \beta_2 x+ \beta_3 y+ \beta_4 x^2 + \beta_5 xy + \beta_6 y^2 + \beta_7 x^2 y + \beta_8 xy^2 \tag{86}$$

respectively, where $\mathbf{\beta_i}$ are constants associated with node **i** [8].

Another important aspect of the finite element analysis is the mapping from local coordinates to global coordinates. This is needed, because a systematic way is required for integrating different elements (sizes and distortion) throughout the meshed model. In order to do this a matrix is used called the Jacobian **J**.

The Jacobian matrix **J** has the form

$$J = \begin{bmatrix} \frac{\partial X}{\partial \xi} & \frac{\partial Y}{\partial \xi} \\ \frac{\partial X}{\partial \eta} & \frac{\partial Y}{\partial \eta} \end{bmatrix} \tag{87}$$

where ξ and η are the local (natural) coordinates, with **X** and **Y** defined as (isoparametric formulation)

$$X = \sum N_i X_i \text{ and } Y = \sum N_i Y_i \tag{88}$$

and**,** $\mathbf{N_i}$ is the shape function for node **i**. Also $\mathbf{X_i}$ & $\mathbf{Y_i}$ are the global coordinates **x** & **y** of node **i**.

The relation between the local and global coordinates is

$$dXdY = |J| \, d\xi d\eta \tag{89}$$

where **|J|** is the determinant of the Jacobian matrix. The determinant of the Jacobian is a constant (scaling factor) if the elements are not distorted, and a function of space as the element gets distorted.

Chapter 3

Results & Discussion

The study modeled three cases of duct acoustics. Each case had the same geometry as mentioned in the introduction but different boundary conditions. The geometry is 3 meters in height and 20 meters long. The boundary conditions for each of the cases was:

- **Case I;** Left Face: Constant Real Pressure Amplitude = 2; Right Face: Impedance = ρc
- **Case II;** Left Face: Constant Real Pressure Amplitude = 2; Right Face: Velocity = 0
- **Case III;** Left Face: Constant Real Pressure Amplitude = 2; Right Face: Pressure = 0

The pressure frequency is held constant at 100 Hz. for all cases in this section. The unit of the **pressure amplitude** is Pascal. The phase speed **c** and mass density ρ are 340 m/s and 1.225 kg/m^3 respectively.

The cases chosen for this study were picked for several reasons. All the cases had a pressure boundary condition on the left face because this boundary condition was satisfied exactly regardless of the level of mesh refinement. Consequently this allowed a constant reference point that all other changes could be measured against.

The boundary conditions on the right were chosen to see the effect different boundary conditions had on the mesh. The right face boundary conditions for the three cases were mixed, natural, and essential boundary conditions respectively.

The corresponding mechanical system for all three cases would be a bar with a constant oscillating force on the left face. For Case I the bar would be of infinite length, for Case 2 the bar would be finite with its right end free, and Case 3 would be a finite bar with its right end fixed.

Another important aspect that must be addressed is that the frequency of 100 Hz. is above the first cut on frequency. This would then imply that the plane wave assumption was no longer true. This would be the case if the boundary conditions on the left and right

side of the duct were not uniform. Since the boundary conditions on this study were all uniform, there were only plane waves created in the duct for all cases.

The consideration of plotting either the real, imaginary, or amplitude of the pressure and velocity fields must also be addressed. This concern applies only for Case I, since Case II & III contained only real or imaginary quantities but never both in the solution field. Consequently the only choice available was to plot that quantity present.

Case I contained both real and imaginary quantities in the pressure and velocity fields. Consequently a choice needed to be made in the quantity to be plotted. Notice that the analytical solution for the imaginary and real quantities of both the pressure and velocity fields are orthogonal and equal in maximum amplitude.

This means that plotting the pressure amplitude or velocity amplitude would have produced constant pressure and velocity fields throughout the domain. Therefore no comparison except for actual amplitude difference could be done. Consequently this choice was ruled out.

The remaining choice was to plot either the real or imaginary or plot both quantities. Plotting both would have been redundant since the only difference between the real and imaginary fields is a phase difference. Therefore it was chosen to plot the real part of the pressure and velocity fields for Case I.

All meshes in this thesis were generated using IDEAS Software. All meshes were analyzed with SYSNOISE Software. The results were then post-processed using IDEAS software. The software gave both pressure and velocity results.

3.1 Finite Element Mesh Refinement Analysis

An important aspect of finite element modeling is the mesh refinement needed to obtain an accurate solution. In acoustics and dynamic systems it is appropriate to talk about elements per wavelength. This is the equivalent of knowing the frequency and the element length.[*]

The main focus of this part of the study was to look at the effects that boundary condition type and the order of the shape function interpolation in the element had on the

[*] We will see in part 3 of this section that although this is common practice, it may not produce satisfactory results.

solution. The section looked at the error between the finite element and analytical solutions for different levels of finite element mesh refinement. The meshes were refined uniformly, so no localized mesh refinement was done.

In this section the elements were not distorted, therefore only the effect of refinement was present. Furthermore the mesh was uniform throughout the domain of the duct (See. Fig. 5.).

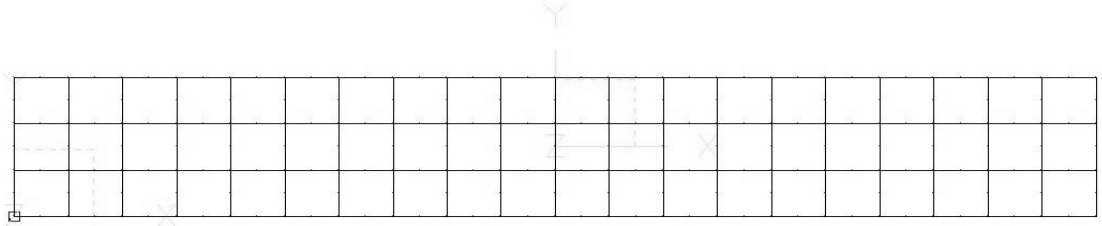

Figure 5. Uniform Mesh.

Figure 6 shows a typical pressure field plot solution. Notice that the wave-front created is plane. This reiterates the assumption that for uniform boundary conditions no cut-on mode will be excited in the duct.

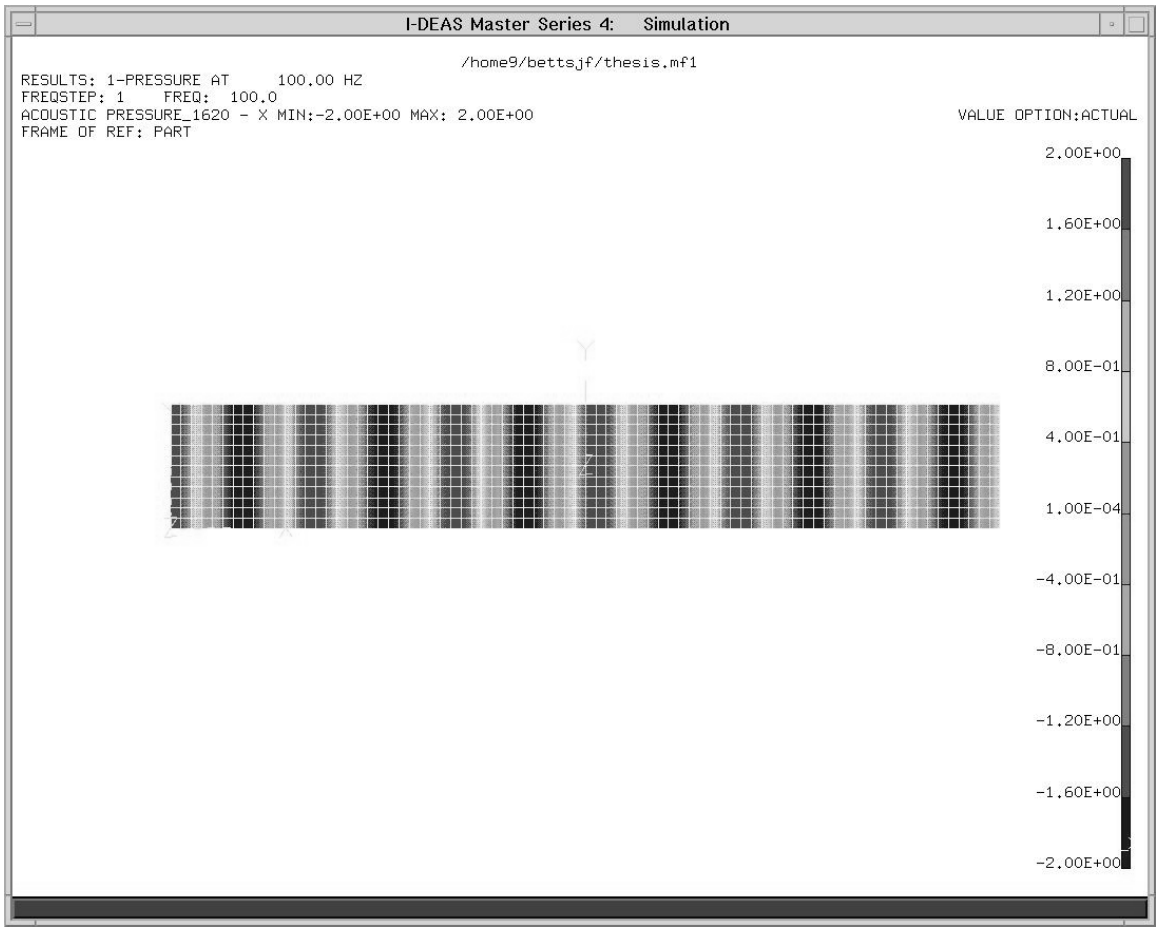

Figure 6. Case I Real Pressure Field Plot for the four-node 13.6 elm/wavelength.

Error plots at different locations in the tube were not included in this section; rather they were placed in Appendix A in order to make the section more readable. Throughout this section these figures will be referenced. The naming convention for these figures is simple. The convention goes as follows: the letter of the appendix precedes the figure number. The figure number in the appendix corresponds to the figure number in the text. For example the error plot associated with **figure 7** in the text is in **appendix A** named **Figure A-7.**

The absolute error was defined by the absolute value of the difference of the analytical and numerical solution divided by the analytical solution and multiplied by 100.

3.1.A. Four-Node Quadrilateral Element Pressure Frequency Response for Case I

Figure 7. shows the four-node element frequency response for Case I. As expected the finer meshes approximated the analytical solution better.

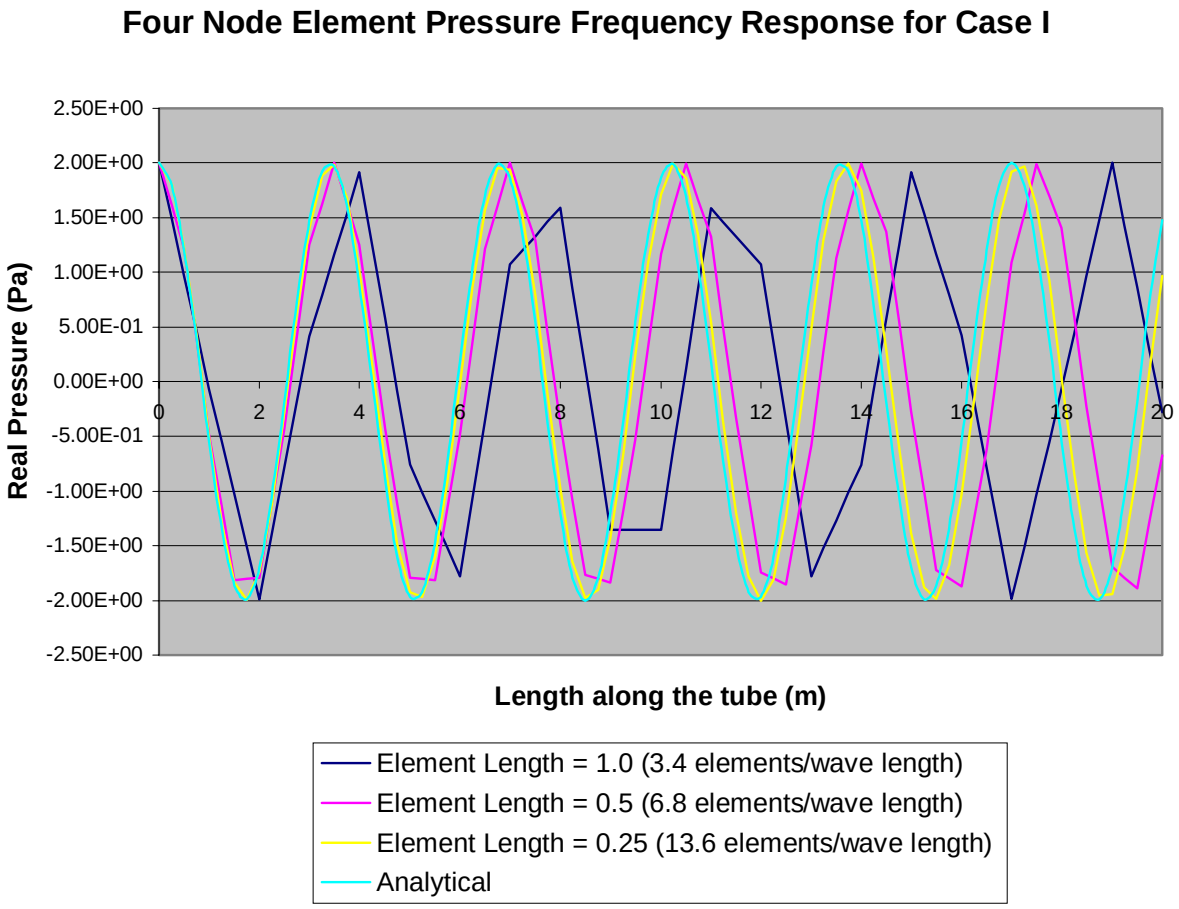

Figure 7. Four Node Element Pressure Frequency Response for Case I

Notice that close to the pressure boundary condition (near x = 0 m) the analytical and finite element solution match very closely even for a relatively coarse mesh (3.4 elements/wave). At positions away from the boundary condition, a greater degree of mesh refinement was needed to continue to attain an accurate solution.

This trend can be explained. The pressure boundary condition on the left face is an essential boundary condition and the solution independent variable. The essential boundary conditions are forced upon the matrix solution. Consequently, close to the face with the essential boundary condition, the solution must start at that value.

The natural boundary conditions on the other hand are satisfied through mesh refinement. The impedance boundary condition on the right face involves a relation with velocity and consequently it is a natural boundary condition. Therefore by increasing the number of elements per wavelength, the analytical and finite element solution matched more closely on the face of the natural boundary conditions.

To quantify the above trends Fig. A-6 summarizes the percent errors at different locations along the x-axis vs. number of elements per wavelength. The percent errors are very high, exceeding 50% absolute value except for the highest level of mesh refinement and up to 30% there. The figure also shows the general trend of decreasing percent error with increasing mesh refinement. Notice though, that further mesh refinement would be needed to achieve satisfactory results with this type of element and case.

3.1. B. Eight-Node Quadrilateral Element Pressure Frequency Response for Case I

The four-node quadrilateral did not match very well the analytical solution even for very fine meshes. It was expected that the eight-node element would perform better, since the assumed solution within the eight-node element is quadratic. The quadratic assumed solution was expected to be a better match to the actual sinusoidal field. The reason for this expectation was that the higher order polynomial would have an easier time approximating the curvature of the sinusoidal solution.

Figure 8. shows the eight-node element pressure frequency response for Case I. As seen from the graph the finite element and analytical solution match was improved dramatically.

Figure A-8. also shows the dramatic improvement in terms of solution accuracy by using the eight-node vs. the four-node element. The percent errors dropped to less than 5% much faster than for the four-node element. Another important characteristic of the eight-node element was that its solution seemed not only accurate but also much less prone to propagation error. This aspect of the eight-node element makes it very valuable.

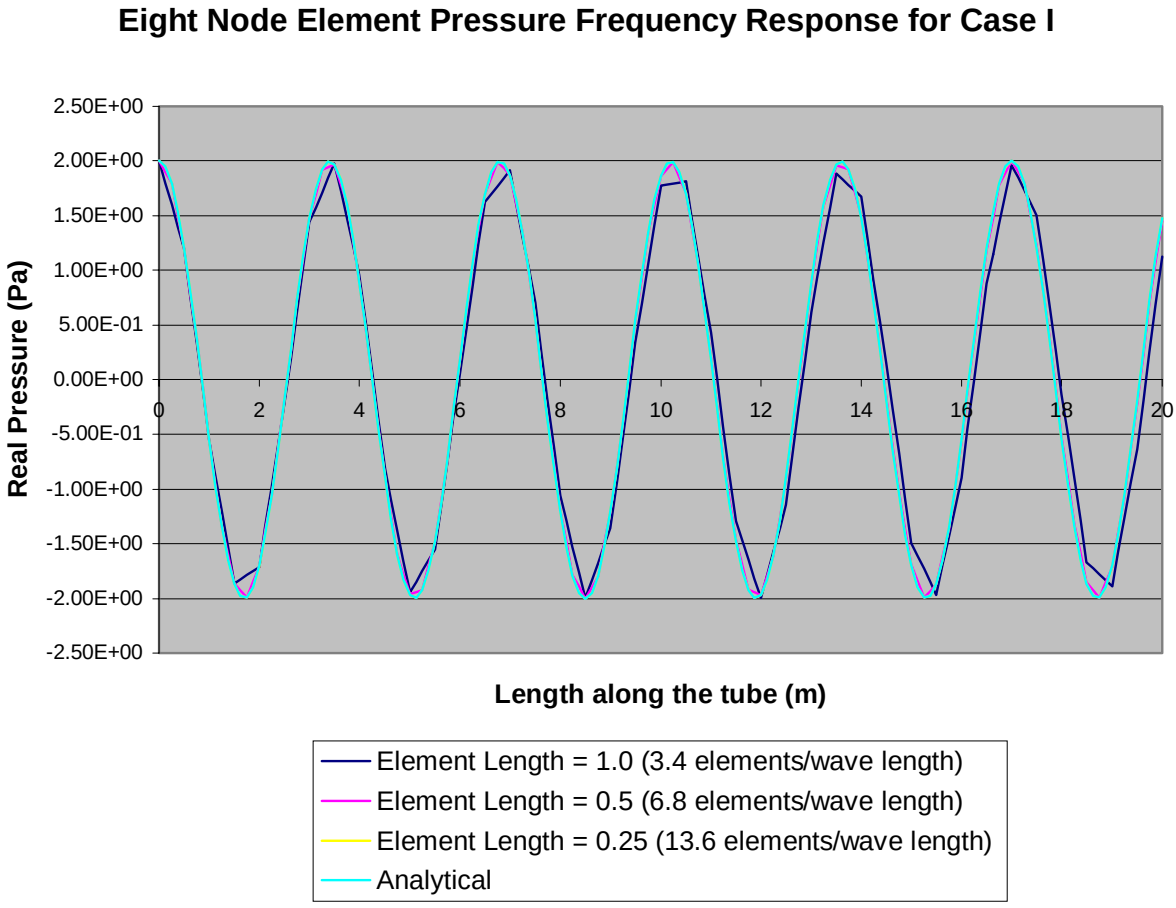

Figure 8. Eight Node Element Pressure Frequency Response for Case I.

3.1.C. Four Node Quadrilateral Element Velocity Frequency Response for Case I

Figure 9. shows the velocity frequency response for the undistorted four-node quadrilateral for Case I. The solution accuracy of the natural solution (velocity) field was different from that of the essential (pressure). The maximum amplitudes of the velocity field tended to decrease away from the analytical solution as the mesh became coarser, rather than stay the same as in the pressure field.

The corresponding velocity boundary condition on the left face due to the pressure boundary condition (essential) was not matched exactly as in the pressure field. Nevertheless the velocity boundary condition was better matched at the left face than the corresponding velocity boundary condition on the right face due to the impedance condition.

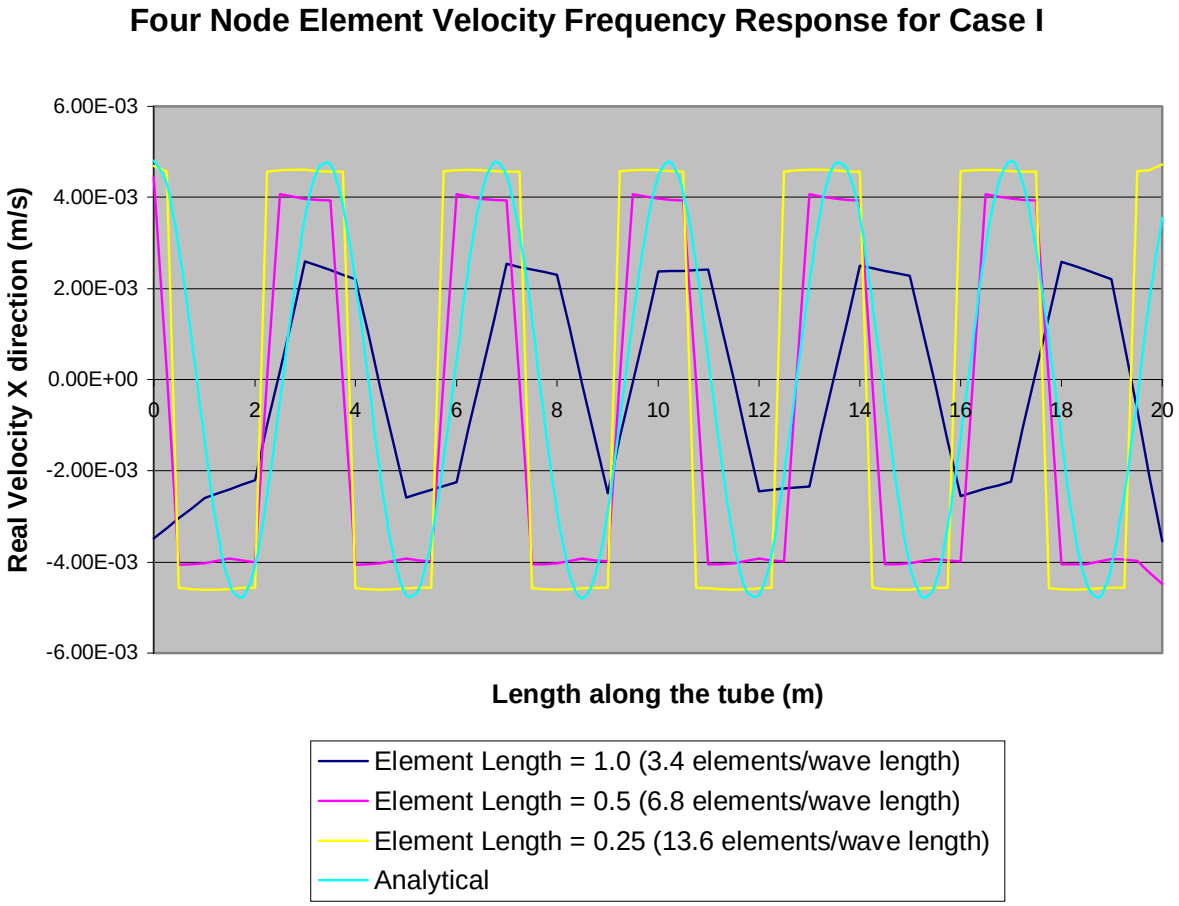

Figure 9. Four Node Element Velocity Frequency Response for Case I.

Another important aspect of this plot was that the velocity field was square oscillatory even for the finest mesh rather than sinusoidal as the analytical solution. This result was unique for this case. The author does not understand why this behavior was observed for this case.

Figure A-9. shows the error plot for the four-node velocity frequency response. Comparing the error plots for the pressure and velocity field, it is seen that the error diminished faster for the velocity field than the pressure field when the mesh was refined. Nevertheless the pressure field error approached zero monotonically after about six elements per wavelength, where the velocity field oscillated at around the 10 percent error after about the same number of elements per wavelength.

3.1.D. Eight Node Quadrilateral Element Velocity Frequency Response for Case I

The velocity field was not approached well with the four-node element for this case. Figure 10. shows the eight-node velocity frequency response for Case I. For this element the velocity field still did not match the analytical solution. It is interesting to note that the solution still was square wave like with noise like variability at the peak velocities.

Now looking at the error plot (Fig. A-10) for this element we see that the error decreased monotonically to zero as we increased the number of elements per wavelength. It also suggests that the solution was more location dependent for the velocity field than for the pressure field. The errors varied from a mean of around 40% for a distance **x** equal to 20 meter to around 5% for a distance of 5 meters.

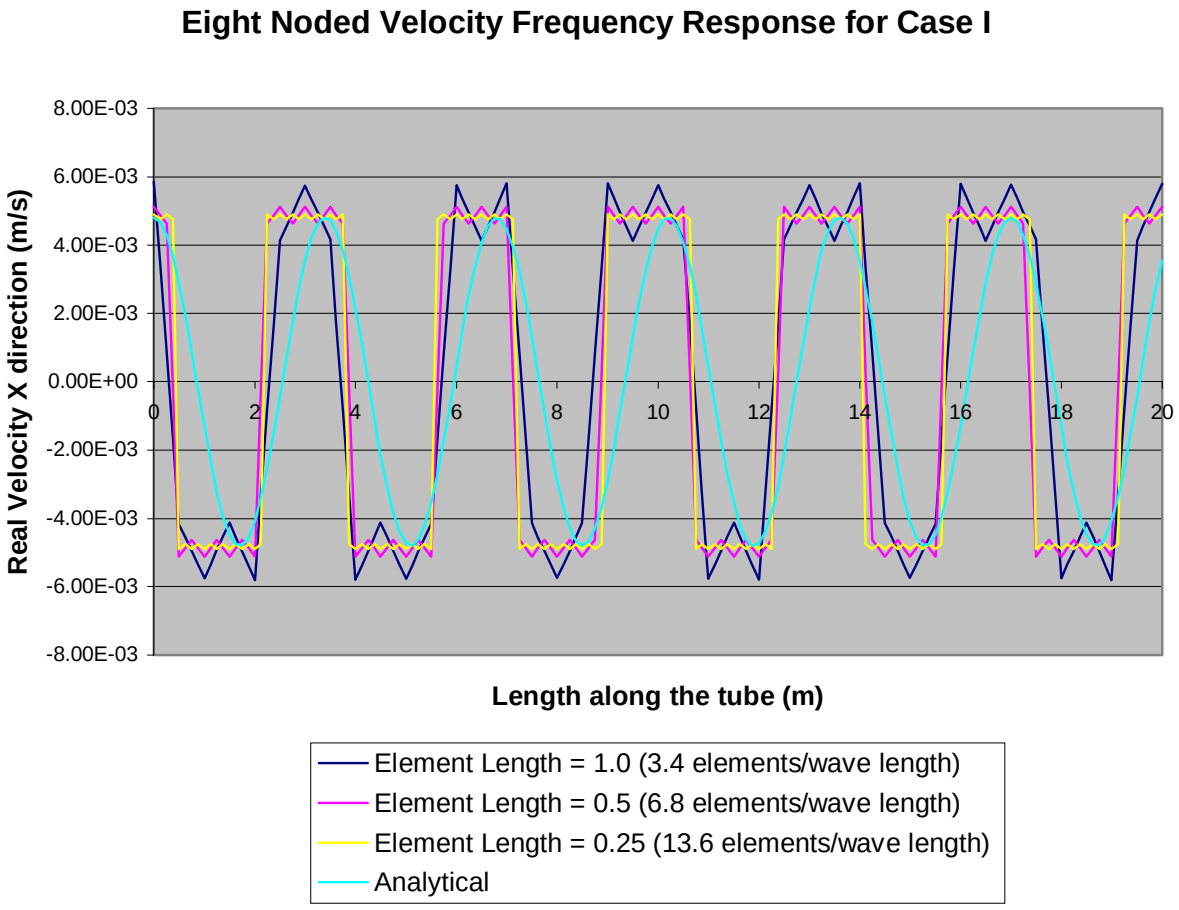

Figure 10 . Eight-Node Element Velocity Frequency Response for Case I at 100 Hz.

3.1.E. Four-Node Quadrilateral Element Pressure Frequency Response for Case II

For Case II a pressure boundary condition (essential) on the left face and a velocity boundary condition (natural) on the right face of the duct was applied. Figure 11. shows the pressure frequency response for the four-node element as a function of the position **x,** along the duct.

Notice that for this case the difference between the analytical and finite element results was relatively constant along length of the duct with little propagation error, and depended mainly on the number of elements per wavelength. Also notice that the amplitudes are higher than the analytical and converge from above.

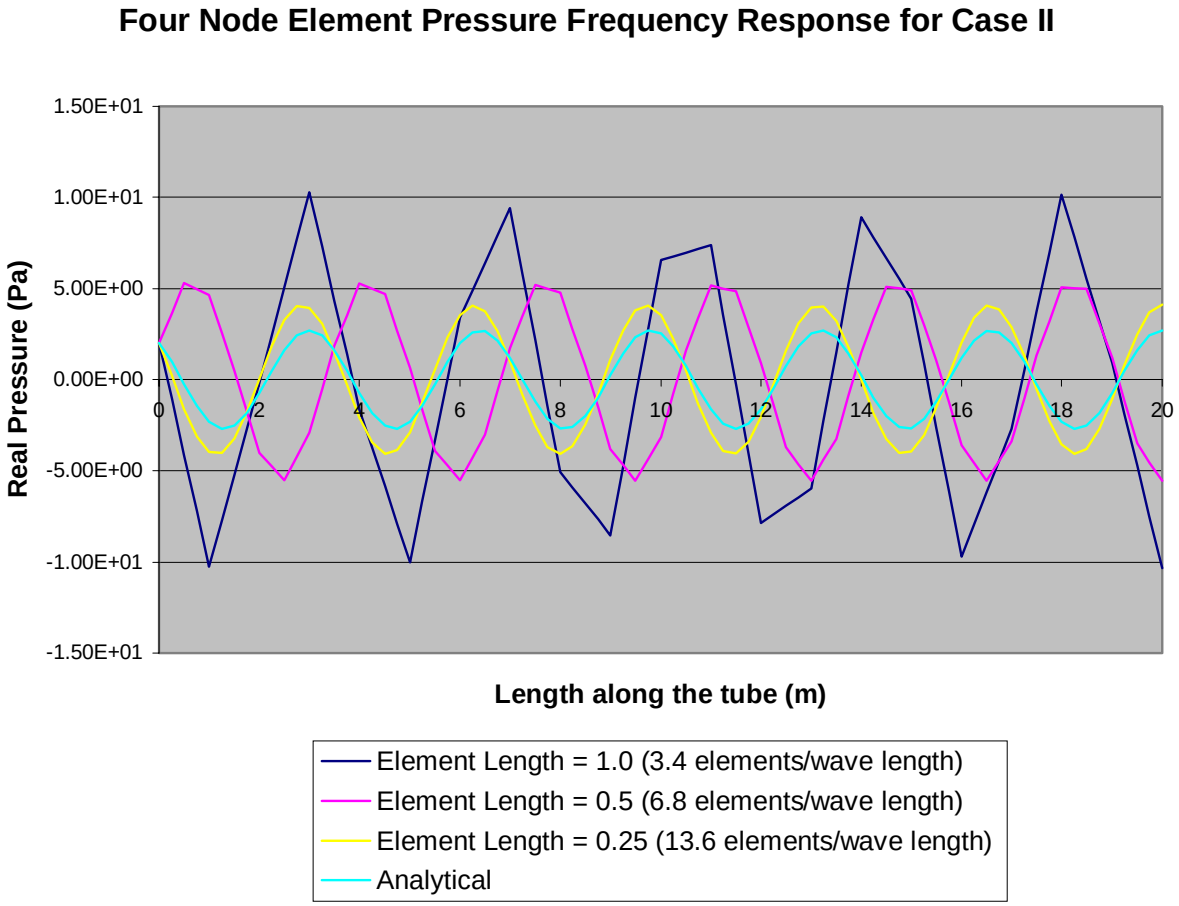

Figure 11. Four-Node Element Velocity Frequency Response for Case II at 100 Hz.

Figure A-11. shows the percent error at different **x** locations for this case. Notice that the percent errors were higher for this case than for Case I for this element. This can be explained because the resultant pressure frequency response was the result of a plane wave traveling in the positive **x** direction and a plane wave traveling in the negative **x** direction. Consequently the FEM method had a harder time approximating this more complicated solution.

3.1.F. Eight-Node Quadrilateral Element Pressure Frequency Response for Case II

It was expected that the eight-node quadrilateral would match better the pressure field than the four-node quadrilateral element. Figure 11. shows the pressure frequency response along the length of the duct for the eight-node quadrilateral for Case II.

The solution match was better for this element than the four-node quadrilateral. The number of elements per wavelength seemed to matter less for this higher order

element. The graph also shows that the solution field for this element was largely independent of the location in the duct.

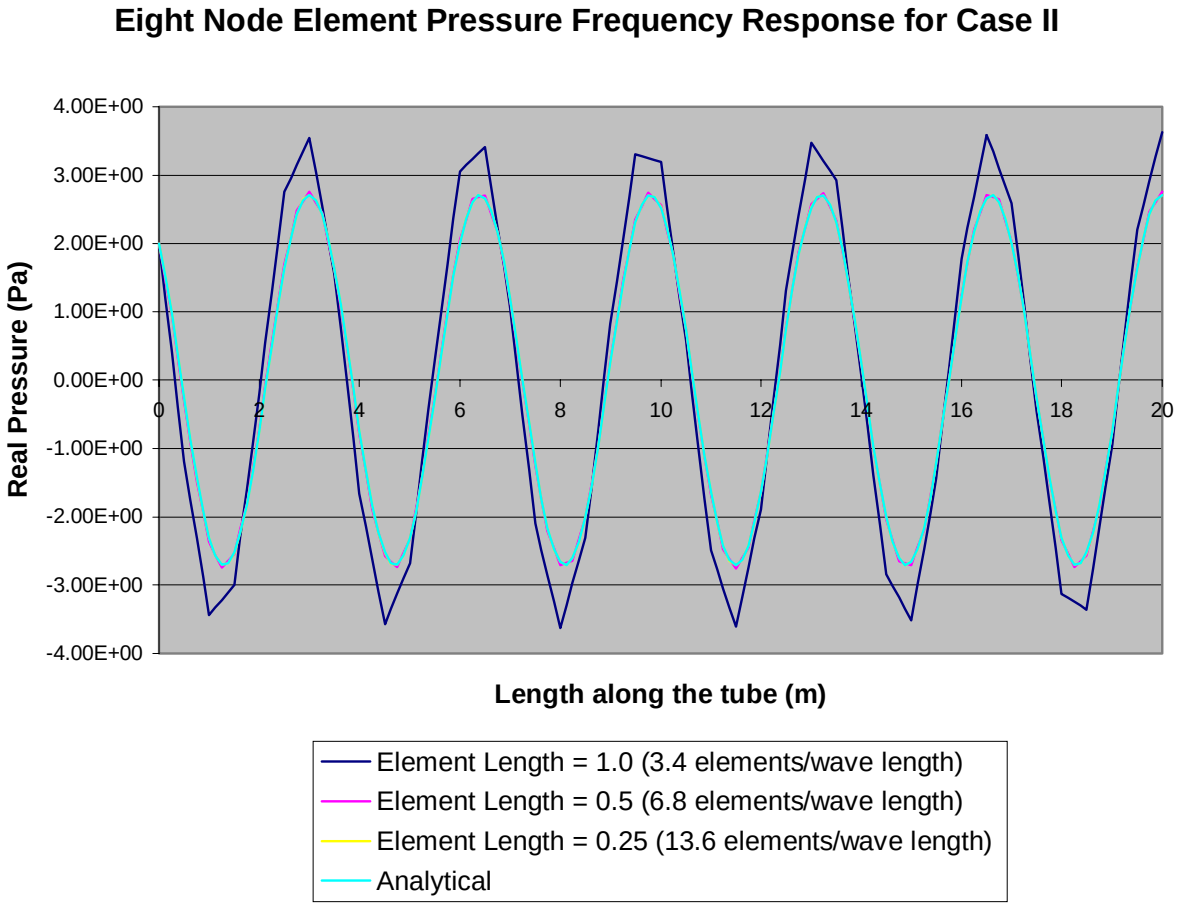

Figure 12. Eight-Node Element Pressure Frequency Response for Case II at 100 Hz.

Figure A-12. shows the percent error at various locations in the duct. Again low errors were present regardless of the number of elements per wavelength and numbers of locations in the duct. The solution field also approached very fast the analytical value and did not change after that. Consequently convergence was achieved faster for the eight-node element vs. the four-node element.

3.1.G. Four-Node Quadrilateral Element Velocity Frequency Response for Case II

Figure 13 shows the velocity frequency response along the length of the duct **x** for the four-node quadrilateral for Case II. The solution was not approximated well by this type of element. Only the finest mesh was capable of "keeping up" with the analytical solution. The coarser meshes had problems with phase, amplitude and frequency of their

solution. No error was plotted since the variation in the solution was too great to achieve any meaningful insight by it.

This figure also shows that the boundary condition, of zero velocity in the right face, was not met, except by the finest mesh. Nevertheless the finest mesh that did approximate this boundary condition correctly, also tended to approximate the rest of the solution relatively well at other points in the duct. Consequently a way of checking whether a mesh is converged is to check to see if we get back the applied natural (velocity) boundary conditions.

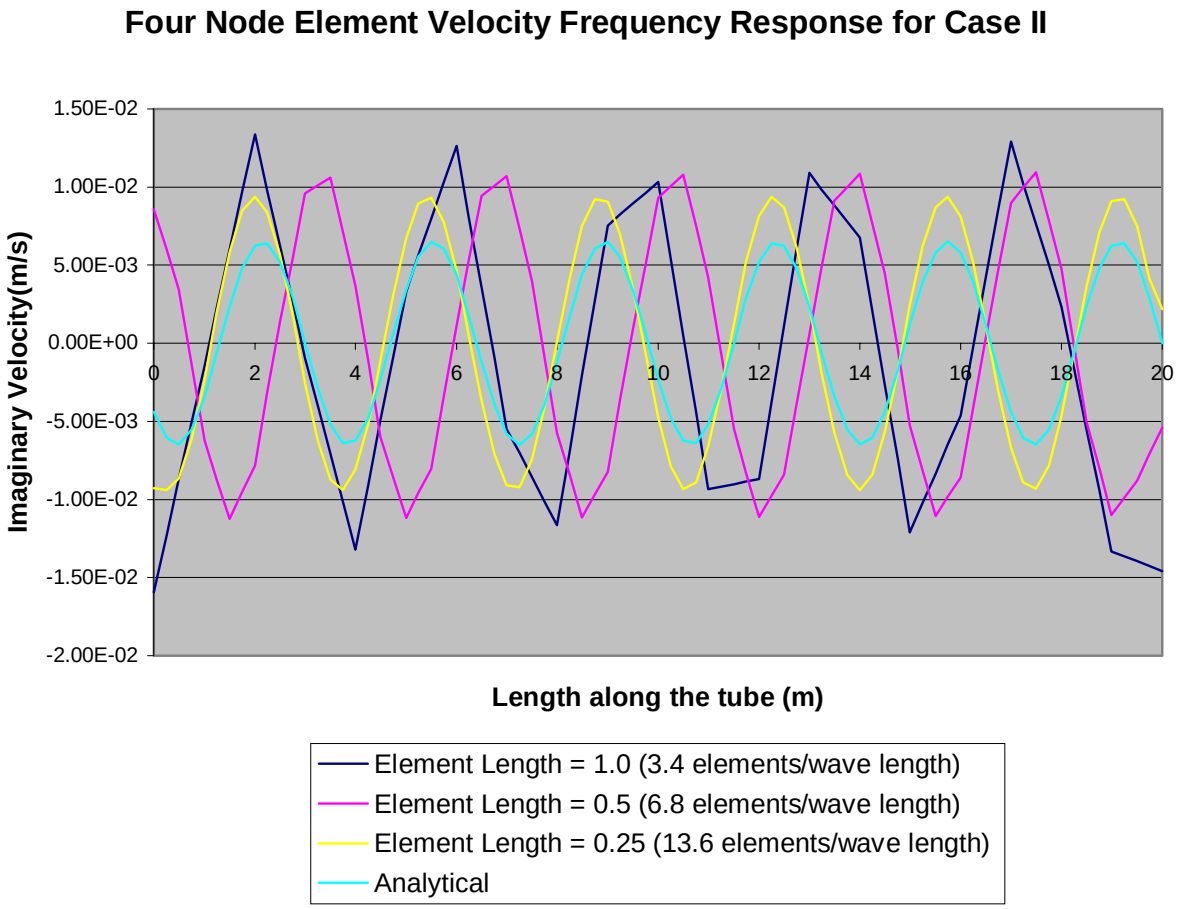

Figure 13. Four-Node Element Velocity Frequency Response for Case II at 100 Hz.

3.1.H. Eight-Node Quadrilateral Element Velocity Frequency Response for Case II

Figure 14. shows the pressure frequency response of this element for Case II. The solution field improved dramatically compared to the four-node element. The velocity boundary condition on the right face was approximated closely. The solution seemed to

be independent of location and tended to vary less with respect to the number of element per wavelength used.

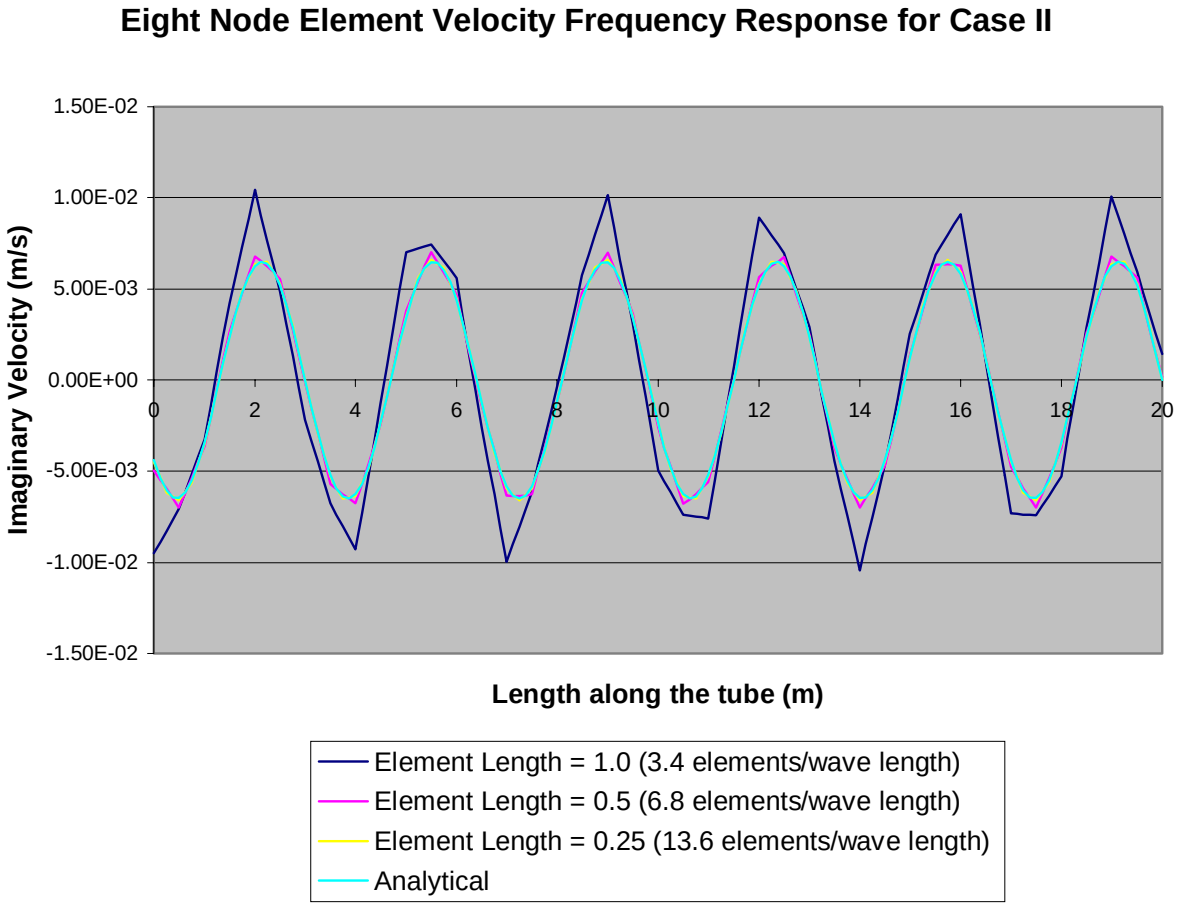

Figure 14. Eight-Node Element Velocity Frequency Response for Case II at 100 Hz.

Another important characteristic from the graph was that the difference in amplitude between the coarser meshes and the analytical solution was more marked. The amplitudes in the coarser meshes were higher than the finer mesh or the analytical solution. This trend was evident throughout Cases I & II.

3.1.I. Four Node Quadrilateral Element Pressure Frequency Response for Case III

Figure 15. shows the pressure frequency response of the four-node element for Case III. The graph shows that both pressure boundary conditions were met exactly as expected (essential boundary conditions).

The solution throughout the tube also improved significantly because of the matching of the boundary condition. The phase and amplitude difference between the finite element and the analytical solution was reduced significantly. The solution tended to agree closer to the analytical solution nearest to both ends where the pressure boundary conditions were present (See Fig. 15 and A-15).

This shows a major difference between meeting the essential vs. the natural boundary conditions. While meeting the essential boundary condition improves the solution in its vicinity, meeting the natural boundary condition improves the solution over the entire solution field given that the elements are about the same size through out the field.

2. Finite Element Distortion Analysis

Another important characteristic that affects the finite element solution is the distortion of the elements. This part of the study was undertaken in order to see the relative stability of the solution field to element distortion. These results were then generalized to predict the increase (or lack of increase) in error for generalized plane wave acoustic fields.

In order to accomplish this part of the study, elements were distorted throughout the length of the duct evenly with the angle between the left face and the element being the distortion angle (See Fig. 16.) This was done in order to avoid errors due to "big" elements being close to "small" element, which would have caused ill conditioning errors rather than mapping errors.

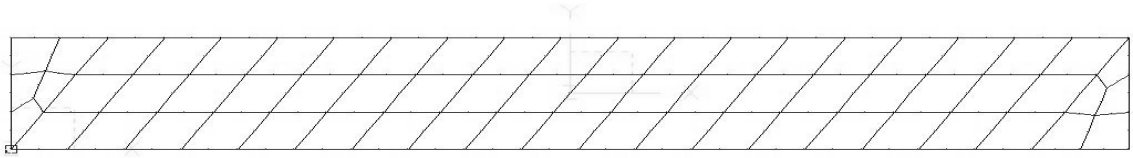

Figure 16. Distorted Mesh.

Rather than looking at errors throughout the duct, error plots were developed for a position in the middle of the duct. There were several reasons for this choice. The solution field was uniformly changing throughout the domain modeled (See Figs. 17 & 18). Further there were five levels of distortion per location.

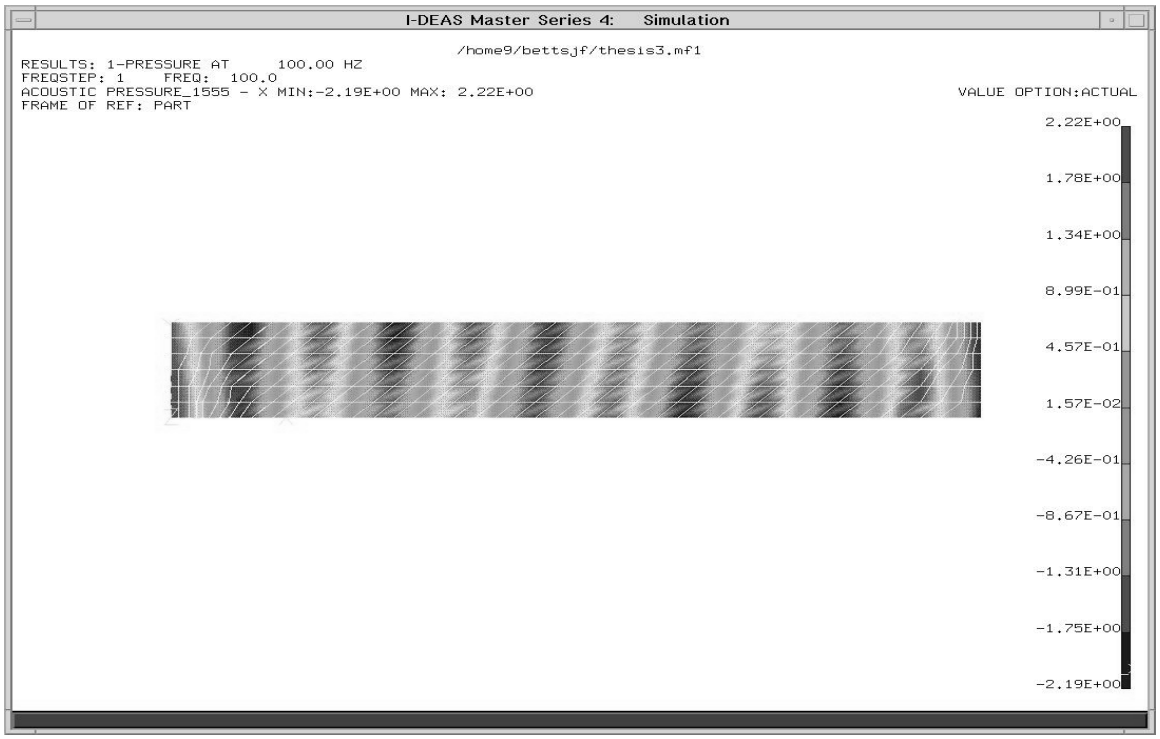

Figure 17. Four-node Real Pressure Field for Case I and 30° degrees distortion at 6.8 elm/wavelength.

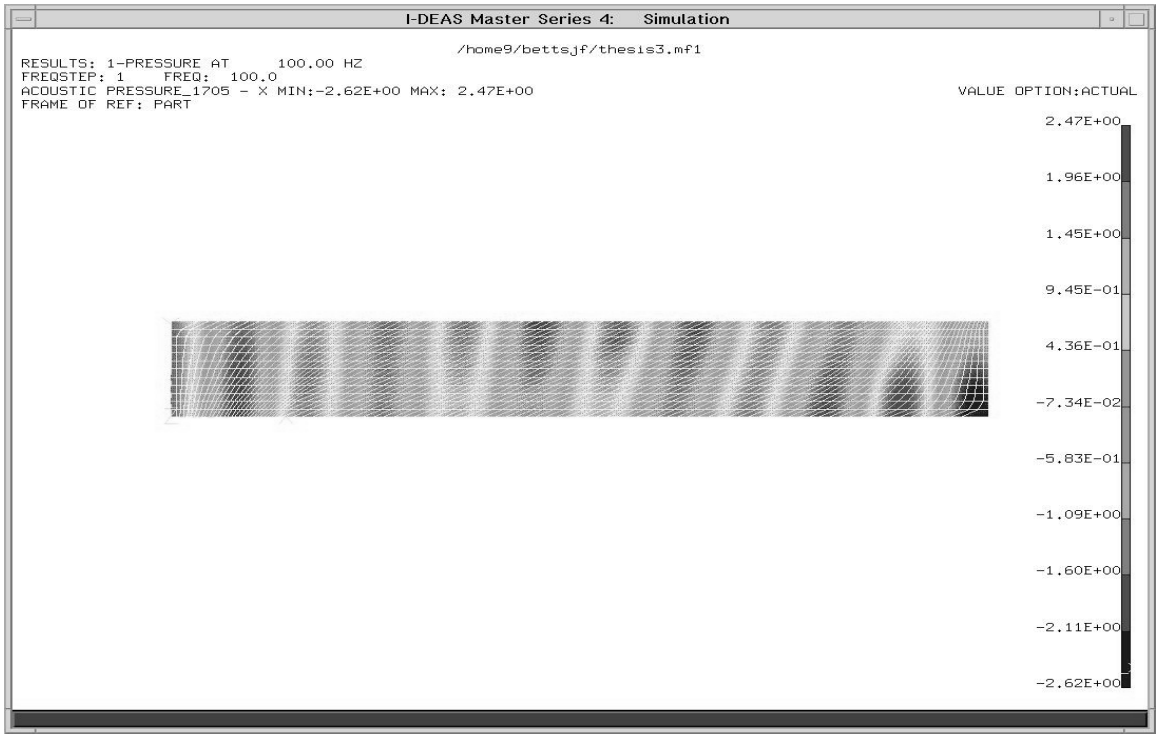

Figure 18. Four-node Real Pressure Field for Case I and 45° degrees distortion at 13.6 element/wavelength.

As the level of elements' distortion increases and its level of refinement decreases, the plane waves in the duct start tilting. Nevertheless the pressure field pattern due to the elements' distortions is repeated throughout the domain. Consequently looking at more points throughout the domain would not have produced more information, just significantly more plots.

It is also important to note that the cut-on mode is not excited in the distorted meshes. Consequently additional errors produced by distortion are solely due to mapping problems and are not due to cut-on mode excitement effects. Appendix B contains additional error plots for this section.

3.2.A. Four-Node Quadrilateral for Case I

Figure 19. shows the pressure frequency response error plot at 100 Hz for this element at different levels of distortion. The first important feature to notice is that up to 30 degrees the results don't seem to differ very much from each other regardless of the of the number of elements per wavelength used.

At 45 degrees a transitioning is observed, where the error does increase significantly at low number of elements per wavelength, and it does not at high number of elements per wavelength. At 60 degrees the error was very high, and it only started to decrease slightly at very high number of elements per wavelength.

The same kind of trend was evident in the velocity field for this element as well as can be observed in Fig. B-19. The transitioning angle nevertheless went from 45 degrees to 60 degrees. To understand this new transitioning angle remember that the velocity field was more accurate than the pressure field for the undistorted configuration (See Sect. Mesh Refinement Analysis). Consequently a higher amount of distortion was necessary for the results to deteriorate.

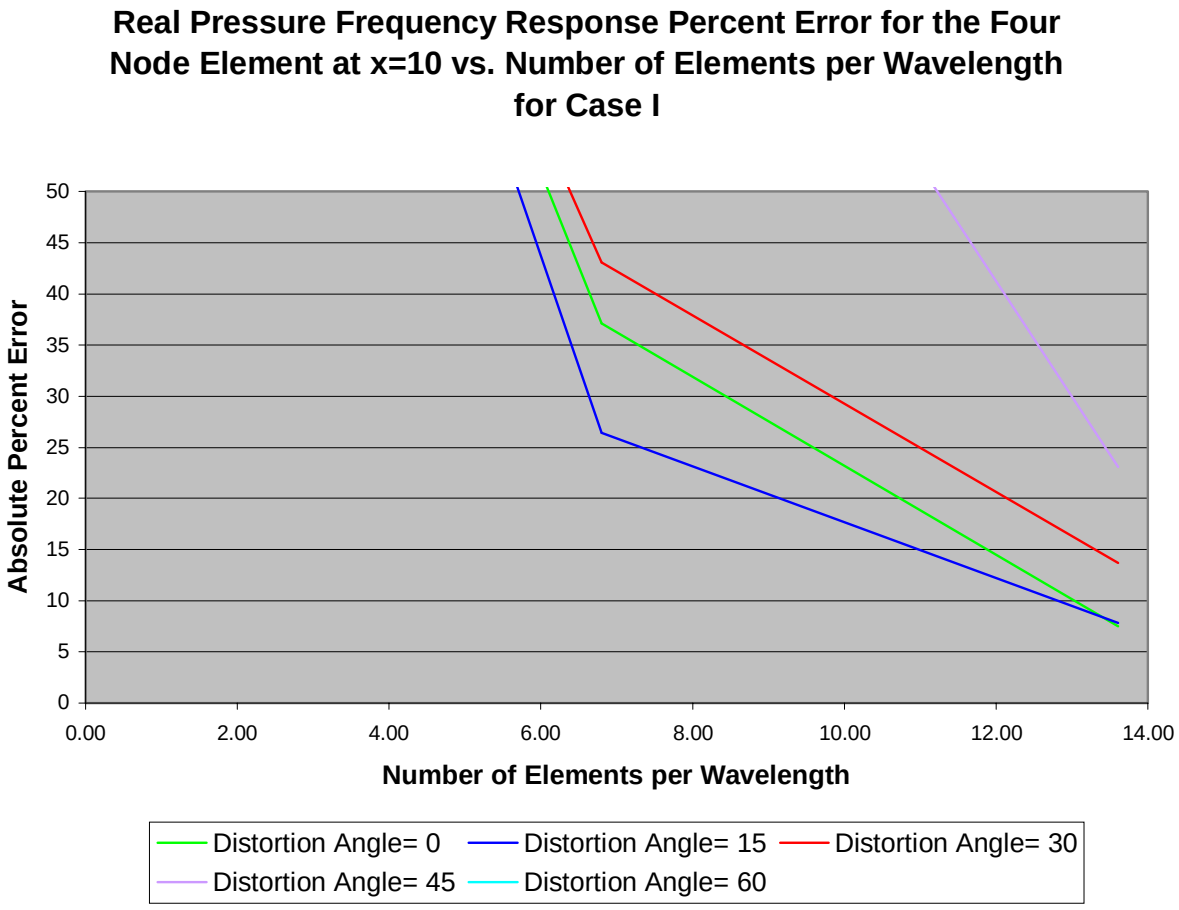

Figure 19. Four-Node Element Pressure Percent Error Response for Case I.*

3.2.B. Eight-Node Quadrilateral for Case I

Figure 20. shows the pressure frequency response error plot at 100 Hz for this element at different levels of distortion. The first difference that is evident from the graph is that the results were less dependent on the amount of element distortion present in contrast to the four-node element. Even at 60 degrees distortion, the model approaches small error after a certain amount of refinement.

* The 60 degrees response is not shown because it is out of range.

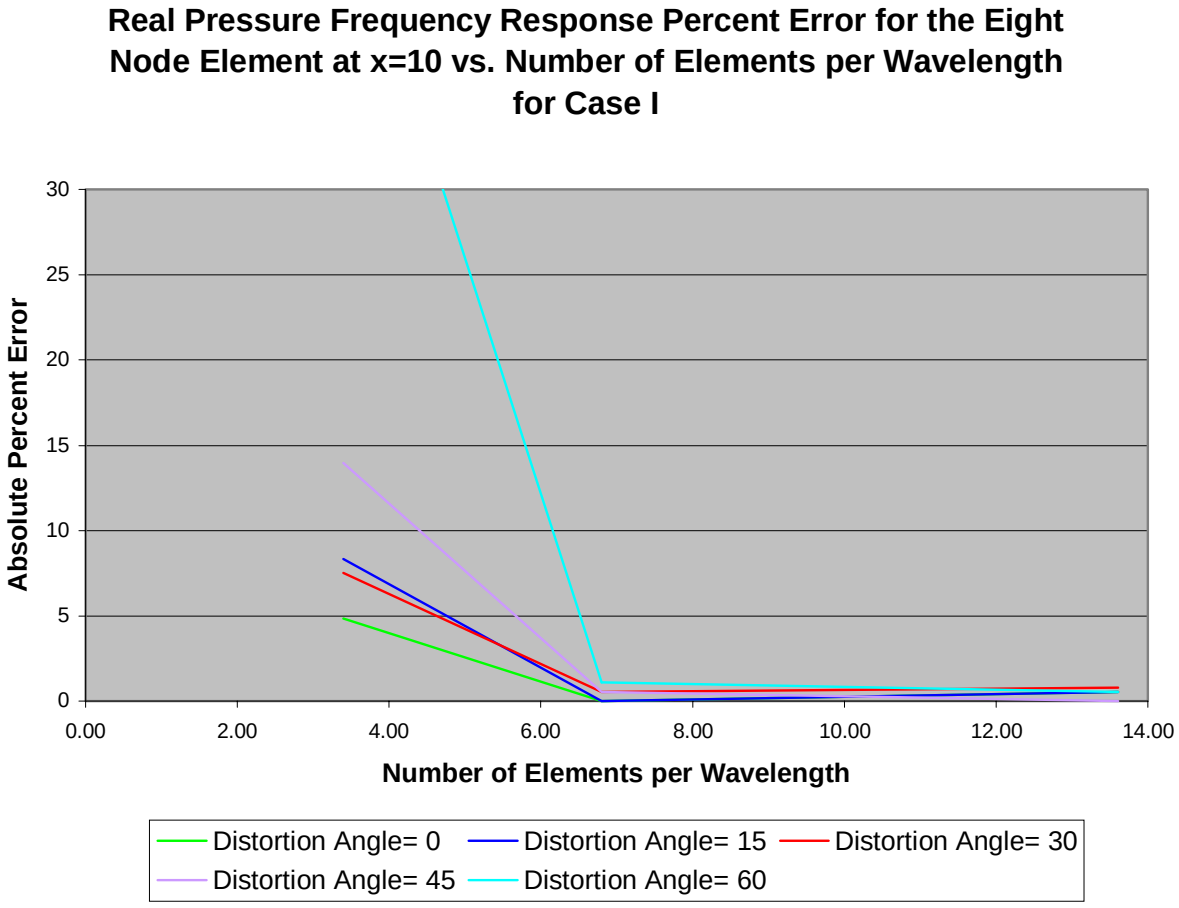

Figure 20. Eight-Node Element Pressure Percent Error Response for Case I.

The velocity field had a less marked difference between the different angles of distortion at the lower number of elements per wavelength as can be observed in Fig. B-20. The difference in the solution continued as the number of elements per wavelength was increased but at a lower rate than the pressure field.

To understand the difference between the four-node and eight-node element in terms of the effect that element distortion had on the solution, the Jacobian needs to be studied. The terms in the Jacobian are basically the order of the respective shape function minus one.** Consequently the determinant of the Jacobian depends on the order of the polynomial used as shape functions.

Since the determinant of the Jacobian is a function of space, the rate of change in space that maps the solution field depends on the order of the interpolating function

** Remember that the terms are differentiated with respect to the natural coordinates.

polynomial. Increasing the distortion angle increases the rate of change within the element that the determinant of the Jacobian must achieve to correctly map the element.

Increasing the order of the interpolating polynomial function within the element increased the capacity of the Jacobian to map the natural coordinate points to the global coordinates. Therefore the four-node element was more sensitive to element distortion than the eight-node element.

3.2.C. Four-Node Quadrilateral for Case II

Figure 21. shows the pressure frequency response error plot at 100 Hz for this element at different angles of distortion. Recall from the previous section (Finite Element Mesh Refinement Analysis Sect.) that this case and element had very bad solutions. This figure reiterates this finding. The solution varies tremendously among the different elements.

The solution field only drops below 100 percent error for a distortion of 30 degrees or less. This case shows quite clearly how errors due to the element's inability to approximate the solution field couple with the Jacobian's incapacity to map the natural coordinates to the global coordinates.

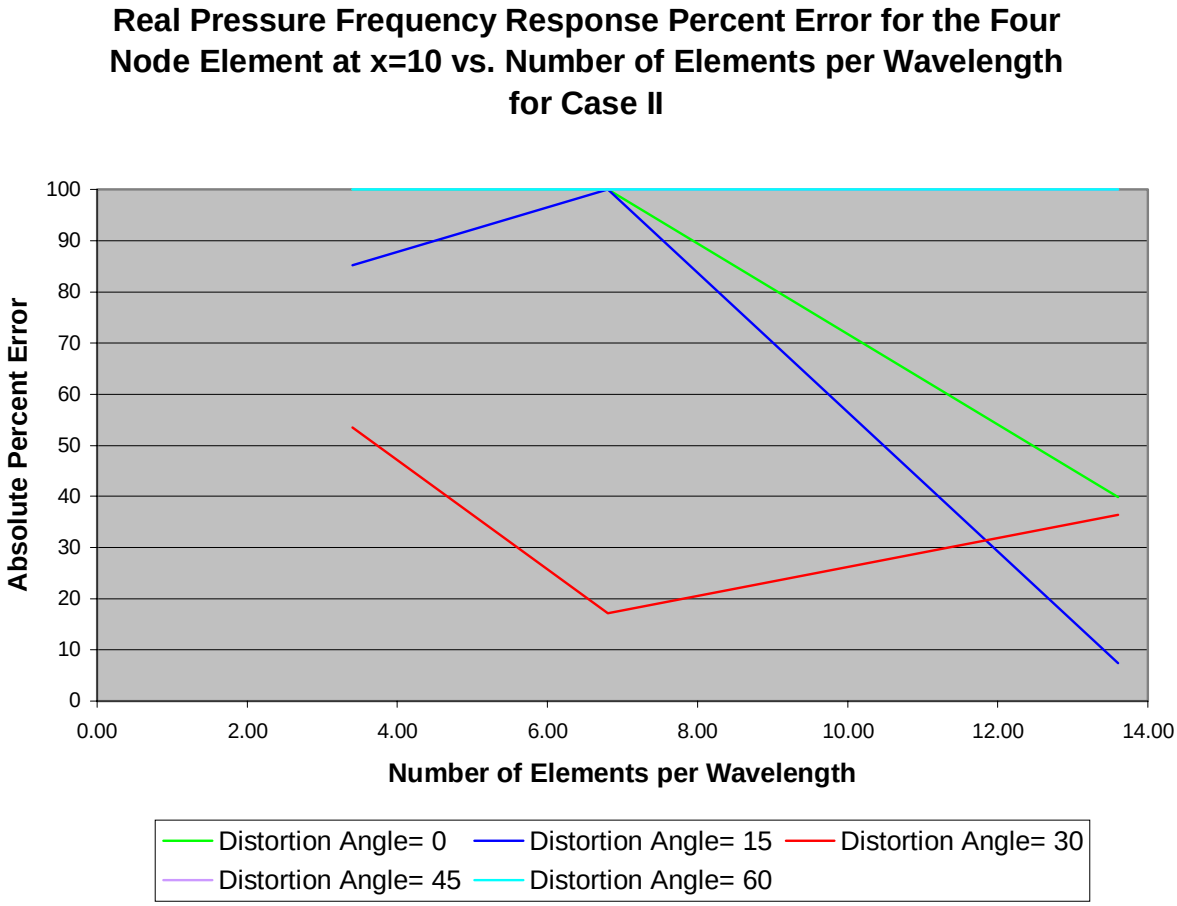

Figure 21. Four-Node Element Pressure Percent Error Response for Case II.

3.2.D. Eight-Node Quadrilateral for Case II

Figure 22. shows the pressure frequency response error plot at 100 Hz for this element at different angles of distortion. Here the picture is similar to that of Case I. At low levels of element distortion the number of elements per wavelength had a marked effect, yet at high number of elements per wavelength the element's distortion becomes irrelevant in terms of solution accuracy.

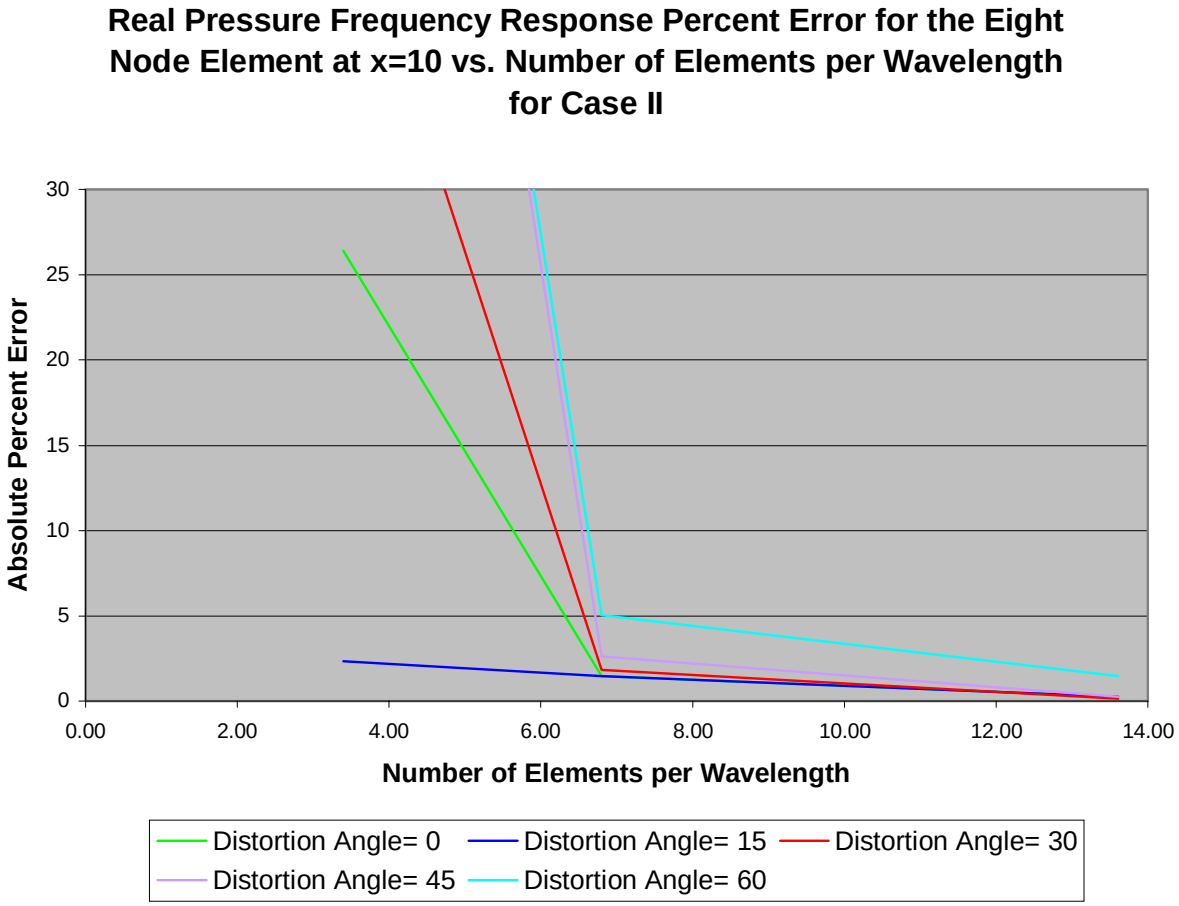

Figure 22. Eight-Node Element Pressure Percent Error Response for Case II.

Another important characteristic that may be puzzling some readers is the fact that as the interpolating shape function polynomials are increased, so is the order of the integration in terms of mass and stiffness matrix that needs to be performed. The results suggest that the improvements in solution approximation as well as improvements in the ability of the Jacobian to map natural to global coordinates out weigh any inaccuracy that may be introduced due to integration inaccuracy.

3.2.E. Four-Node Quadrilateral for Case III

Figure 23. shows the pressure frequency response error plot at 100 Hz for this element at different angles of distortion. The graph shows that the solution field was better than in Case II as was seen in the Finite Element Mesh Refinement Analysis section. Distorting the element had a scattering effect on the solution field.

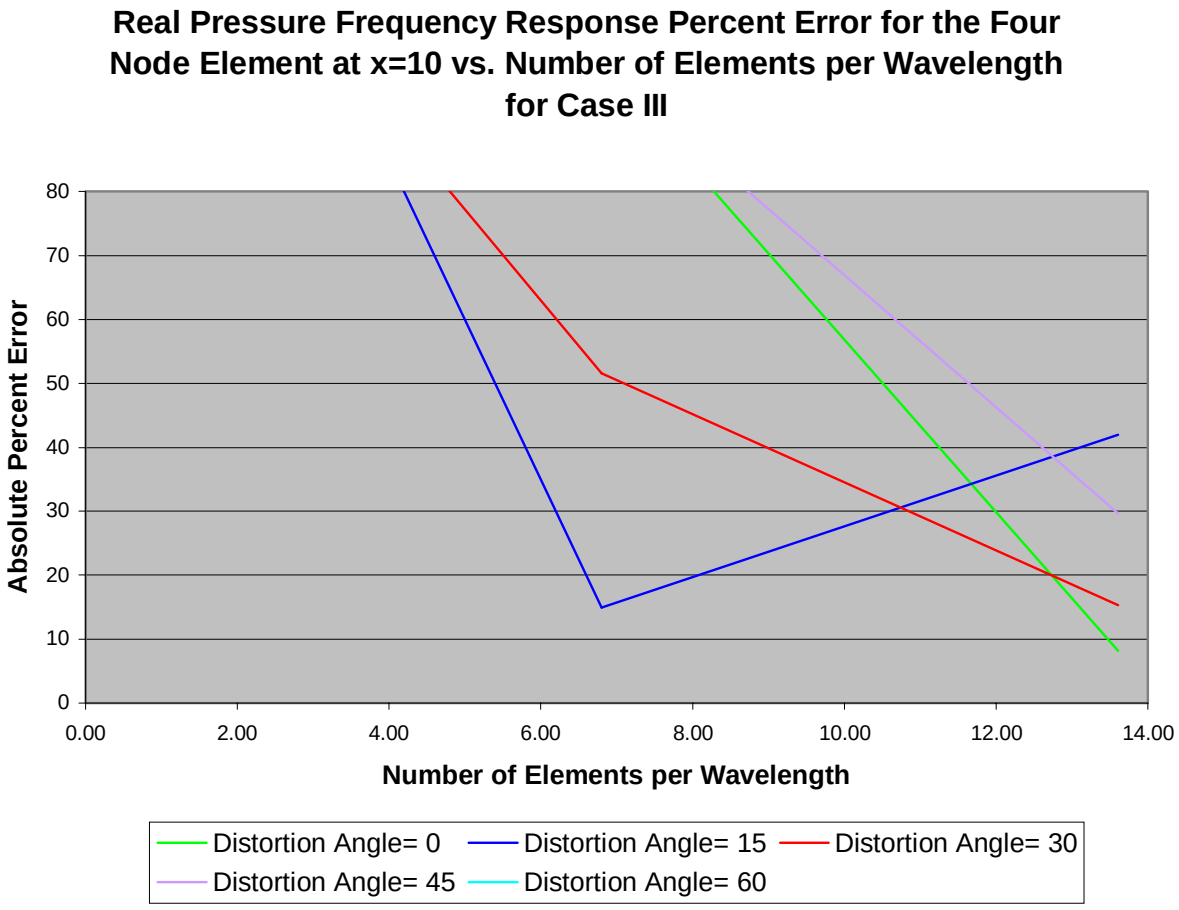

Figure 23. Four-Node Element Pressure Percent Error Response for Case III.

3.2.F. Eight-Node Quadrilateral for Case III

Figure 24. shows the pressure frequency response error plot at 100 Hz for this element at different angles of distortion. Again this graph shows the eight-node element performed better than the four-node element.

Another result that may be perplexing some readers was that the four-node element when distorted produced a scattering of the solution field, without necessarily having the expected higher errors for the highest distortions. The eight-node element in the other hand, had the highest errors for the highest element distortion.

To understand this phenomenon, realize that the eight-node element already had good results at zero distortion. Therefore distorting the element only introduced errors due to mapping and consequently the expected higher error for higher distortion.

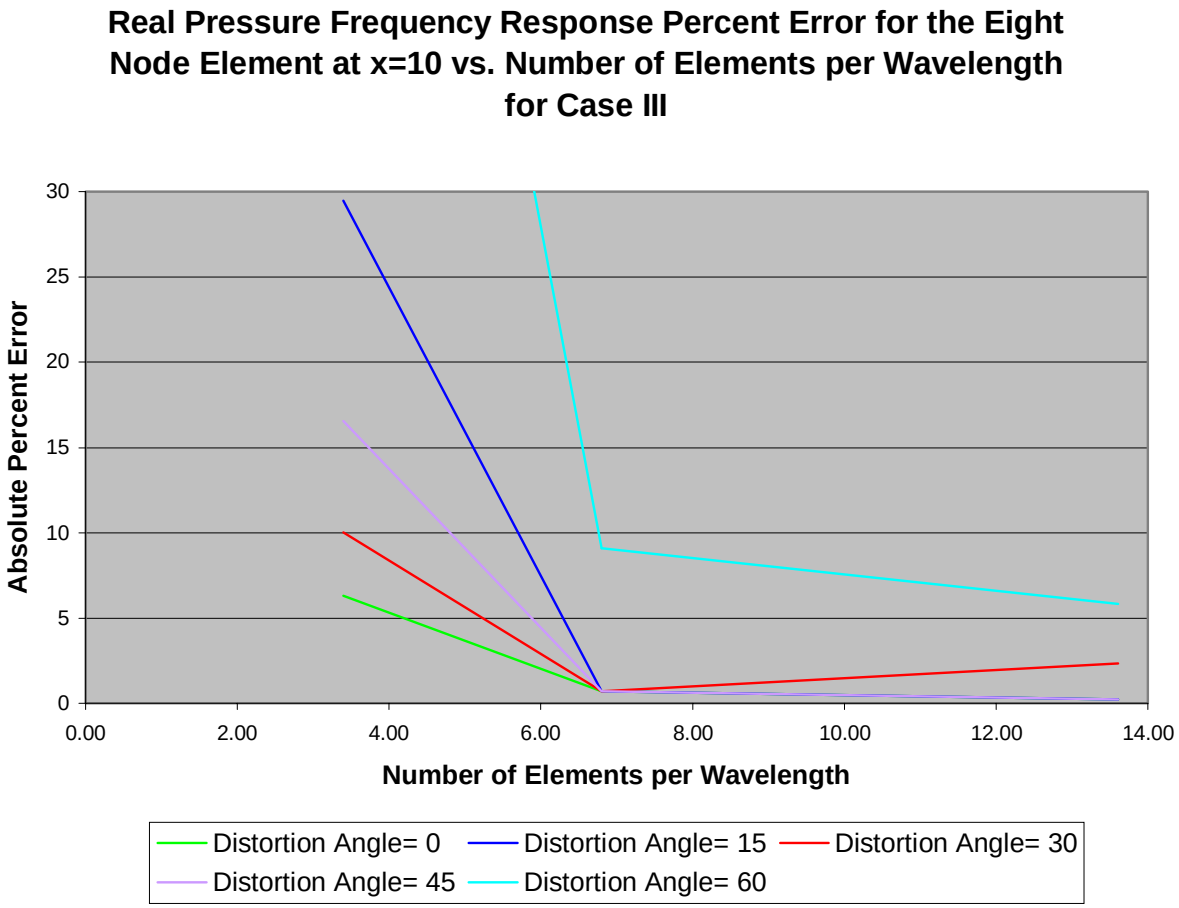

Figure 24. Eight-Node Element Pressure Percent Error Response for Case III.

The four-node element in the other hand already contained errors of refinement for a zero distortion angle. Therefore when the element was distorted, the element now contained errors in mapping and refinement. These new errors in mapping may sometimes cancel previous errors in refinement. Consequently some distorted meshes had lower overall errors.

Nevertheless it is important to note that as the element was distorted to near 60 degrees, mapping errors started to dominate the error field and consequently any canceling with the mesh refinement error became small in the total error of the mesh.

3. Finite Element Mesh Refinement Analysis at Variable Frequency

In the first section on mesh refinement knowing the frequency and the element length fixed the number of elements per wavelength. Throughout this study error plots and response solutions were plotted at a frequency of 100 Hz.

The question then arises, if the number of elements per wavelength was fixed would increasing the frequency (correcting the element length every time) cause higher errors? It is a common practice to use the number of elements per wavelength as a mesh guide [3]. Consequently the likely answer would be that the error should not increase.

With this mentality in mind this study originally fixed the element length of the mesh and changed the frequency to get different number of elements per wavelength. Contrary to expectations some meshes with a higher number of elements per wavelength but higher frequency had larger errors than corresponding meshes with lower number of elements per wavelength and lower frequency.

This section is dedicated mainly to explain this phenomenon, so rather than go through every case and element an explanation is offered as to why this phenomenon occurs. Figure 25. shows pressure frequency response error at the middle of the duct at 100 and 200 Hz for Case I. Notice that the two hundred frequency curve did not lie on top of the 100 Hz curve but rather it was much higher. The reason for this phenomenon is not totally obvious. In order to understand this apparent contradiction, the analytical solution for plane wave acoustics in a duct may be examined.

The analytical solution for case I (See Sect. Analytical Solutions) looking only at changes in pressure with respect to space was

$$p(x)= Ae^{i(-kx)} \tag{90}$$

Taking the first and second derivatives with respect to space, and knowing that $k=\omega/c$ and $\omega=2\pi f$ produces

$$\frac{dp}{dx} = \frac{2A\pi f}{c} e^{-ikx} \tag{91}$$

$$\frac{d^2p}{dx^2} = A(\frac{2\pi f}{c})^2 e^{-ikx} \qquad (92)$$

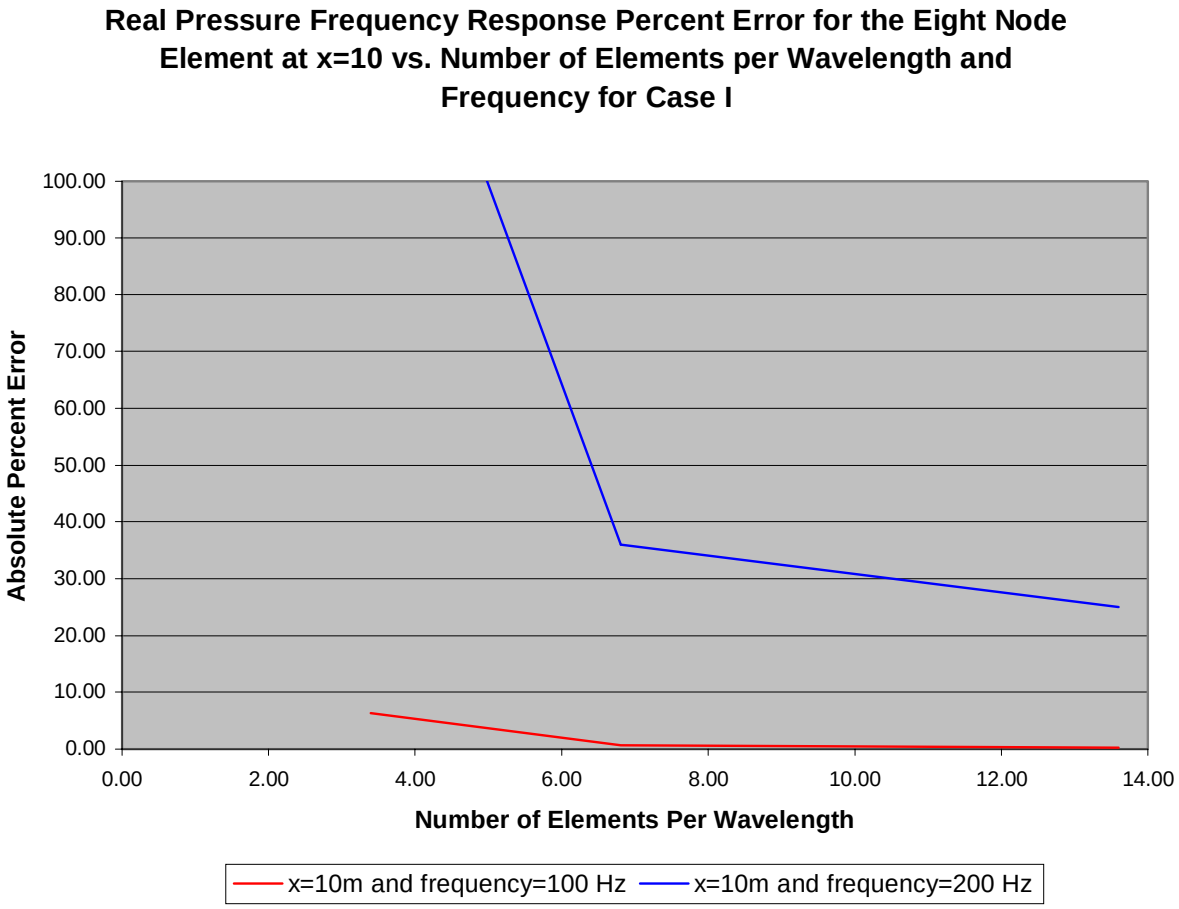

Figure 25. Eight-Node Pressure Percent Error Response for Case I at 100 & 200Hz.

The first derivative is the slope of the pressure field curve. The second derivative is the rate of change of the slope. From the above equations the changing frequency changes the slope linearly, but the rate of change of that slope varies by the square change of the frequency.

The finite element method is trying to approximate the pressure field through the use of the shape functions. As we take derivatives of the shape functions we are essentially decreasing its polynomial order and therefore requiring a higher refinement to

approximate the analytical solution field. At the same time the spatial rate of change of the solution field is increasing every time the frequency is increased.

Therefore increasing the frequency makes it harder for the shape function to approximate the rate of change of the solution field. Also remember that the pressure field and its derivatives are point functions. Hence it does not matter if a certain number of elements per wavelength is fixed. To maintain similar accuracy mesh refinement should increase with the square of the frequency ratio.

This phenomenon leads to a common error by engineers who deal with high frequency problems of blaming the finite element of being inaccurate. The reality is not that the finite element is inaccurate, but that the representation of the field variable over the domain of the element is inadequate to represent the field.

This phenomenon also points to a grave problem with using Lagrange shape functions to model dynamic systems. The use of Lagrange polynomials is appropriate when modeling static solid mechanics problems where even if solution have high gradients, these gradients do not change in space as fast as in dynamics or depend on frequency for that matter.

Another important concept that is important to note from the analytical forms of the solution is that the phase speed c is in the denominator of these equations. The solution field in terms of displacement is of the same form as the one for pressure. Since the phase speed in solids is much bigger than in air, then it affects solid dynamics modeling to a lesser extent than it does acoustic modeling.

Chapter 4

Conclusions and Recomendations

The study showed very decisively that the use of higher order shape function elements better approximate the analytical solution than the lower order shape function element. This was the case for all levels of refinement. The results also showed that the rate of solution improvement due to refinement was much higher in the eight-node element than in the four-node element.

Meeting the natural boundary conditions through mesh refinement was an indication that the mesh was converged. The choice of boundary conditions on the right face affected whether unrefined meshes would overestimate or underestimate the solution field when an essential boundary condition was applied to the left face. In general the use of essential boundary conditions led to an underestimation of the solution field, while the use of natural boundary condition led to an overestimation of the solution field.

The results also showed that throughout the field the pressure field was more accurate than the velocity field. This result was expected since the velocity field comes from the derivatives of the pressure field. The pressure field also tended to approach the analytical solution monotonically while the velocity field tended to vary more in its approach to the analytical solution. This tendency was present regardless of the boundary condition type used.

The element distortion part of the study suggested that the eight-node element was more resistant to increase in error due to element distortion than the four-node element. This was the case regardless of the boundary condition type used. The results also indicated that refinement reduced the sensitivity to element distortion.

The results also showed that the use of the number of elements per wavelength as a meshing guide was inadequate. It concluded that the number of elements per wavelength for good accuracy was frequency dependent.

This study showed that many factors affect the solution accuracy and that correct modeling and convergence is essential in obtaining good results. For the example, the study suggested users verify the model to see if the natural boundary conditions are met.

Users should if possible use higher order elements when faced with complicated solution fields. The user should also expect, at the very least, to retrieve the same natural boundary conditions from the model that were applied to the model, before assuming that the mesh is converged. It is recommended that the user of finite element models should always understand the physical system, and the finite element method and the factors that affect its solution accuracy.

It is recommended that more work be done in the area of developing better shape functions that are more suited for the kinds of solution fields encountered in harmonic problems. The study indicated that the accuracy of the solution greatly depended on these functions.

Appendix A[*]

Finite Element Mesh Refinement Analysis Figures

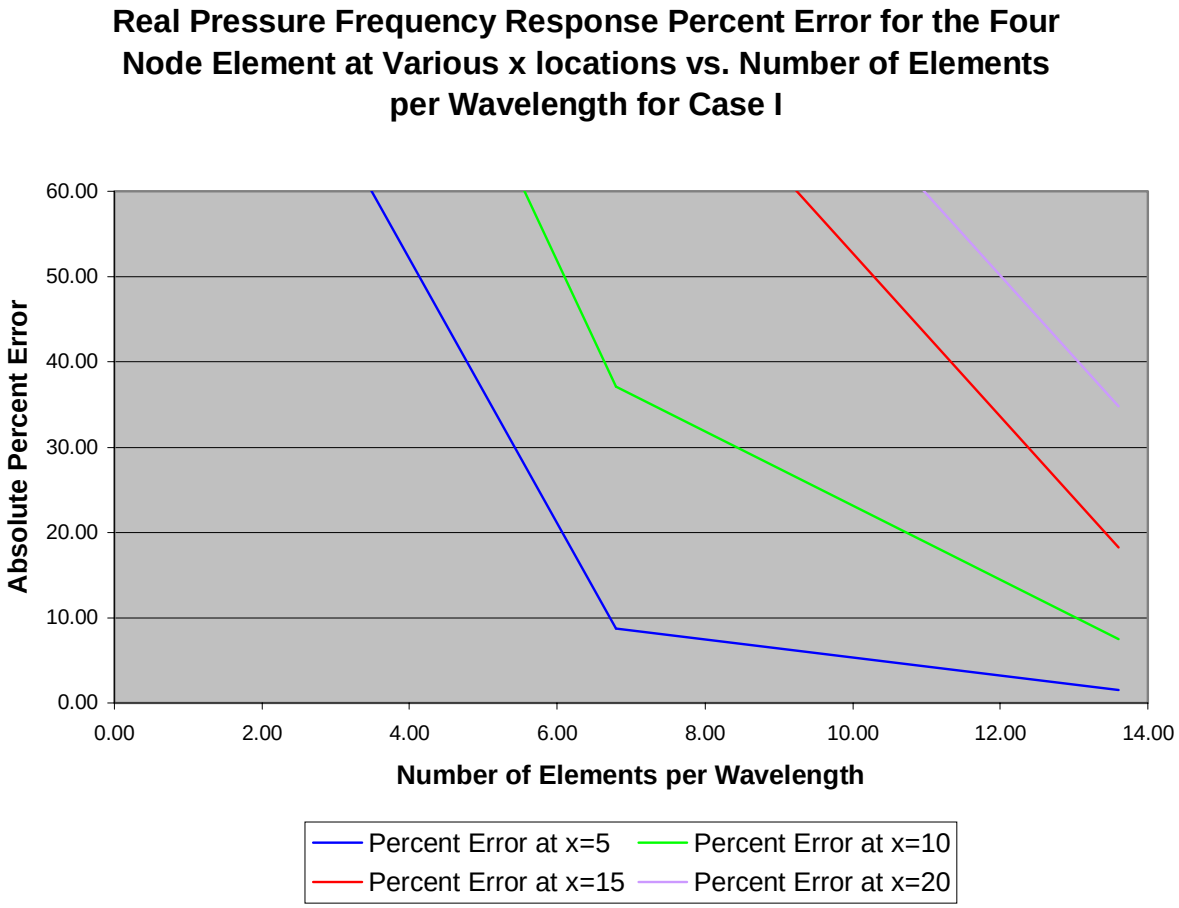

Figure A-7. Real Pressure Frequency Error Response for the Four Node Element for Case I.

[*] The figure numbers in these appendices match the figure number in the text, i.e. Figure A-7. corresponds to Fig. 7 in the text.

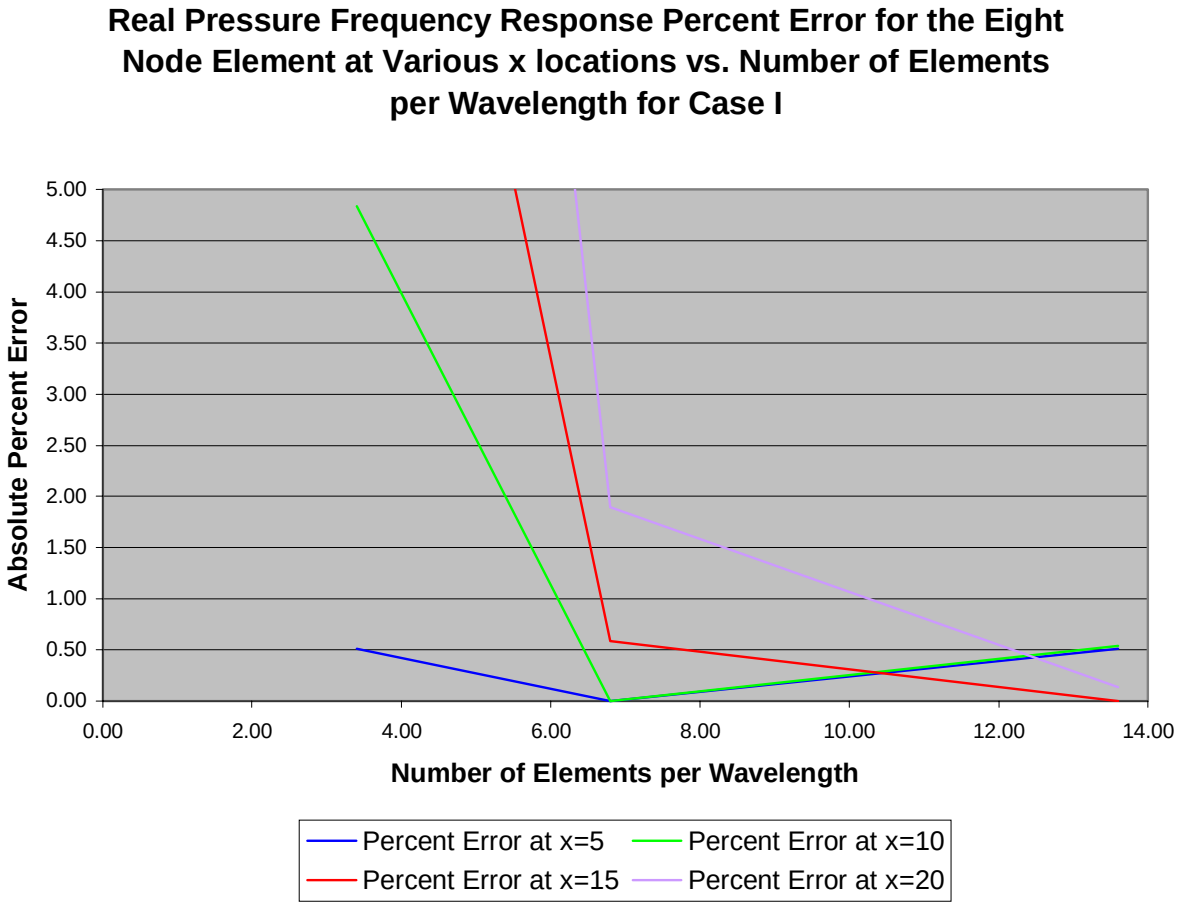

Figure A-8. Real Pressure Frequency Error Response for the Eight Node Element for Case I.

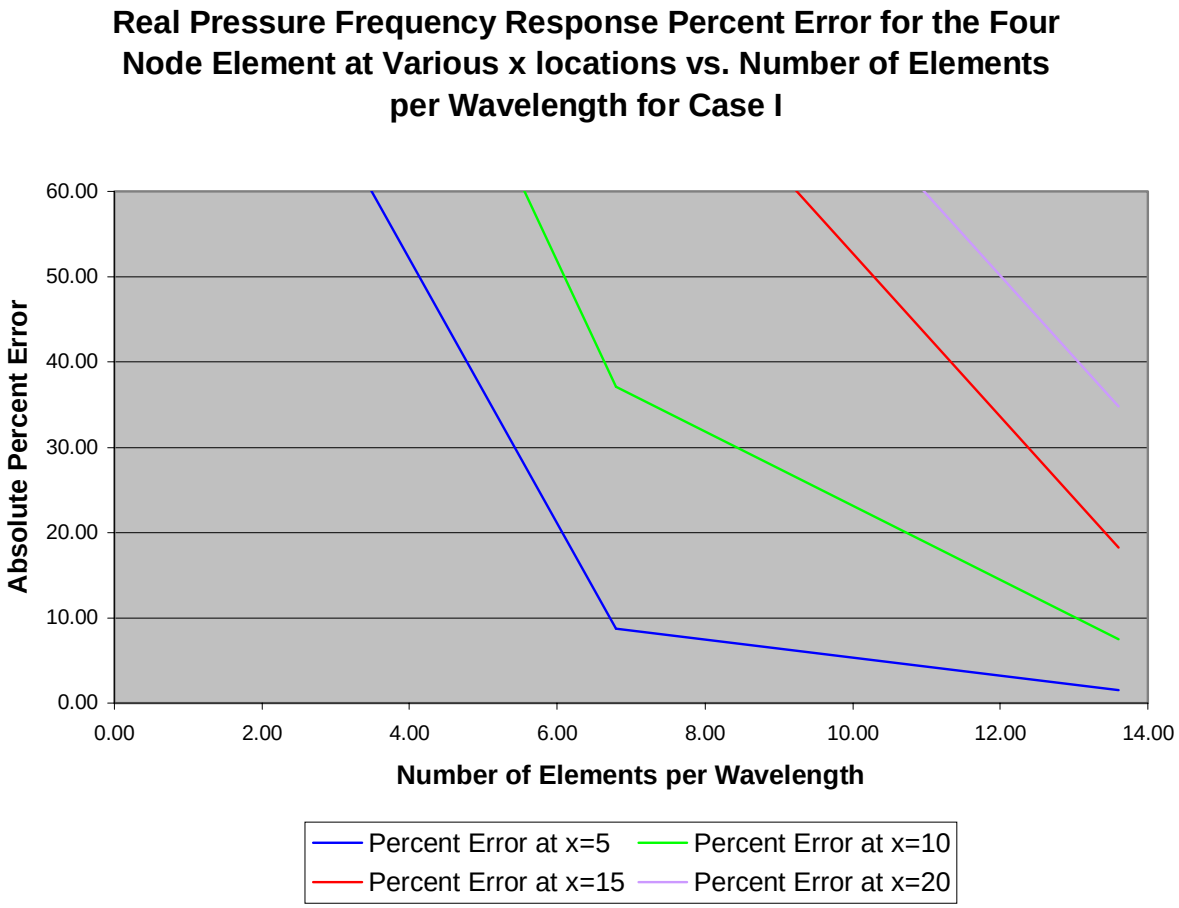

Figure A-9. Real Velocity Frequency Error Response for the Four-Node Element for Case I.

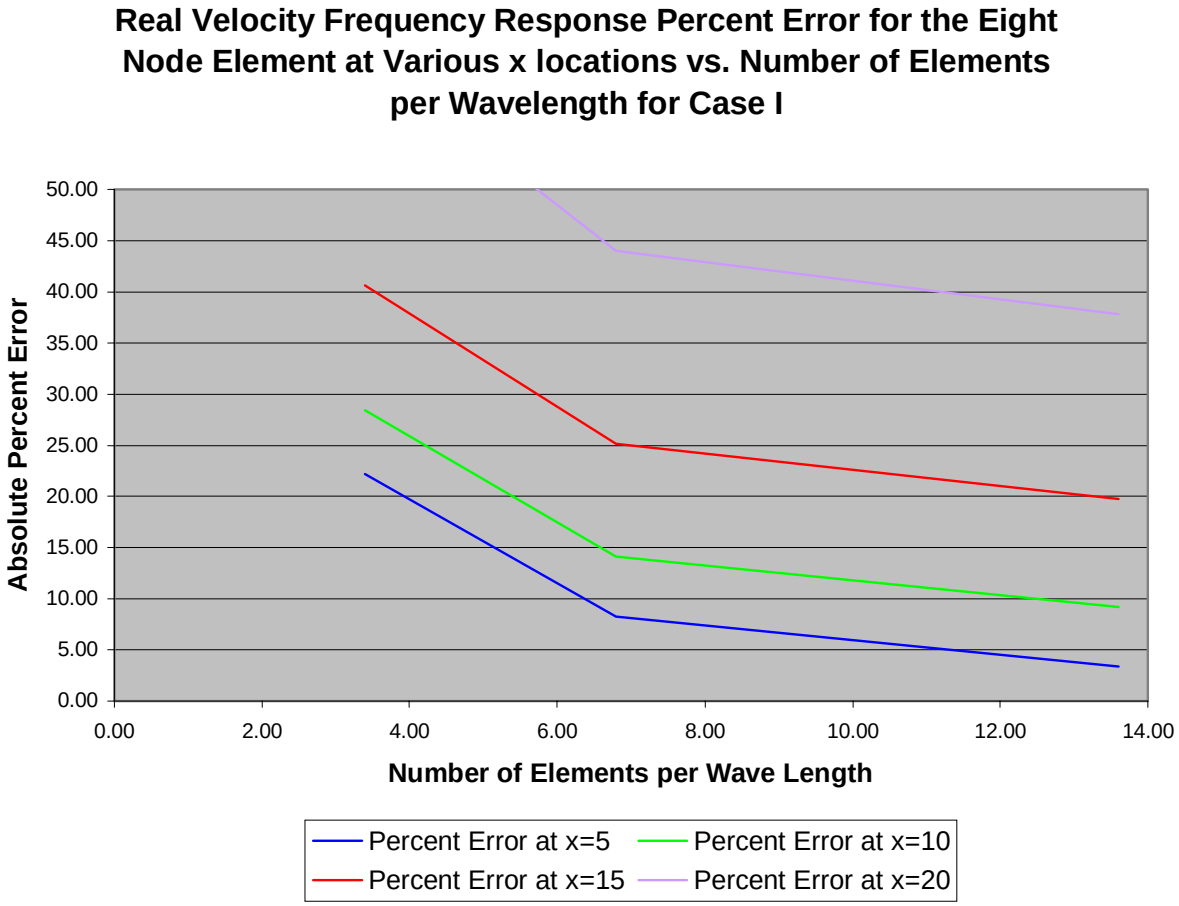

Figure A-10. Real Velocity Frequency Error Response for the Eight Node Element for Case I.

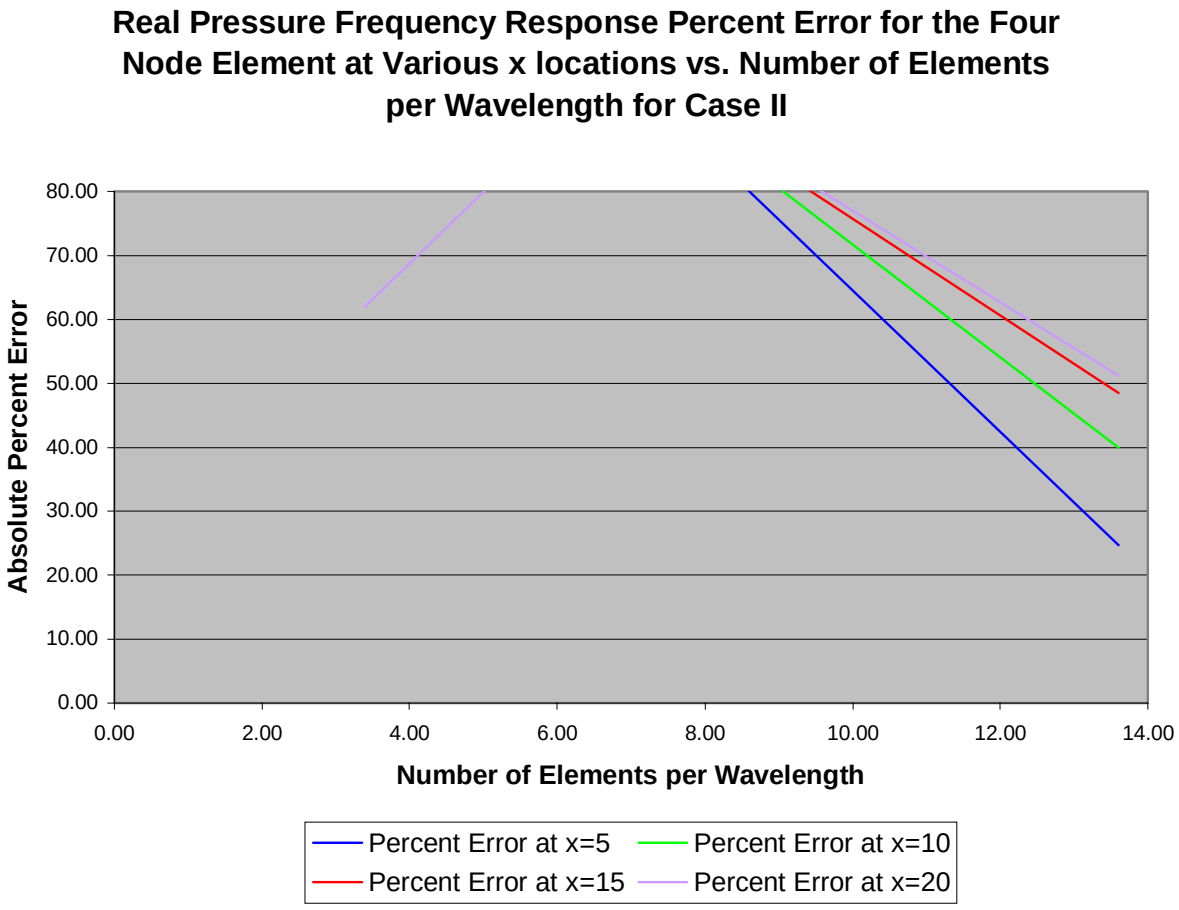

Figure A-11. Real Pressure Frequency Error Response for the Four Node Element for Case II.

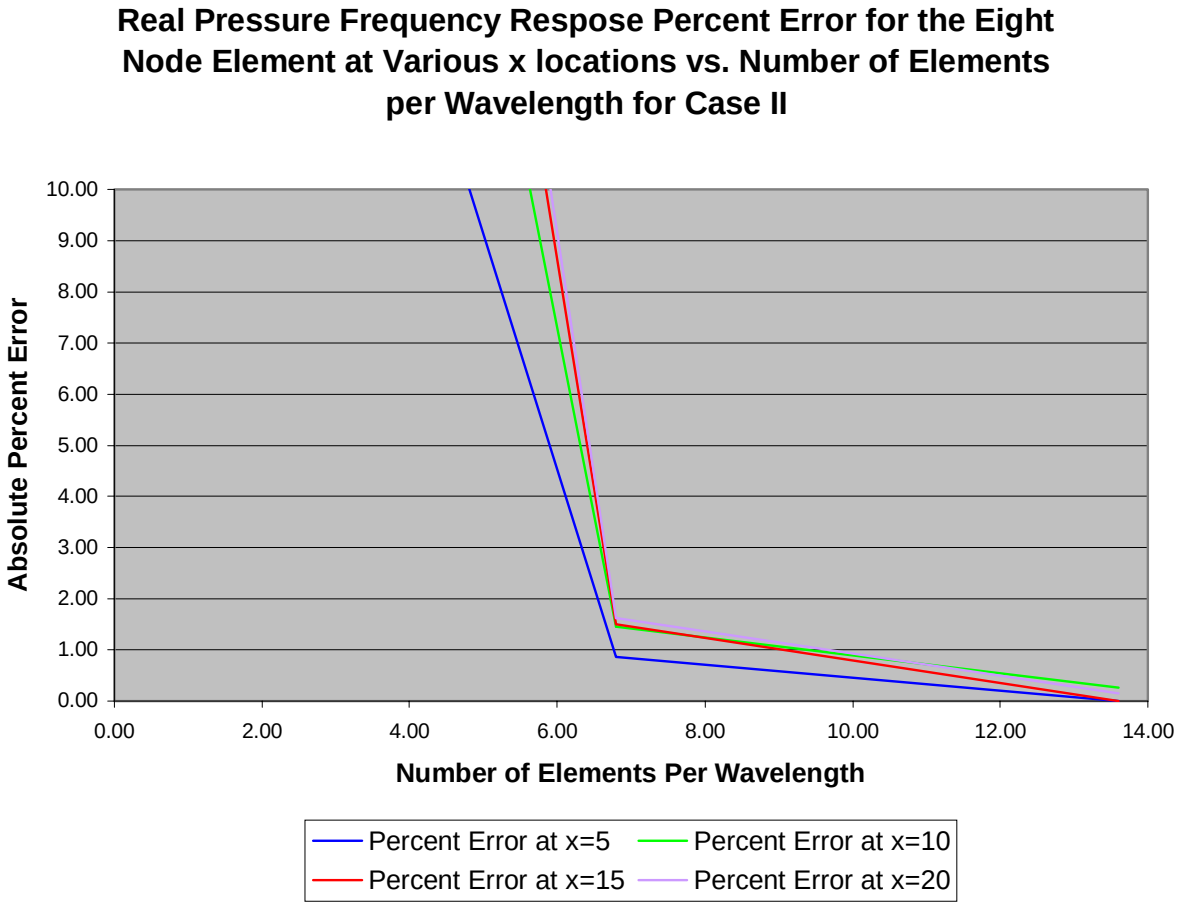

Figure A-12. Real Pressure Frequency Error Response for the Eight Node Element for Case II.

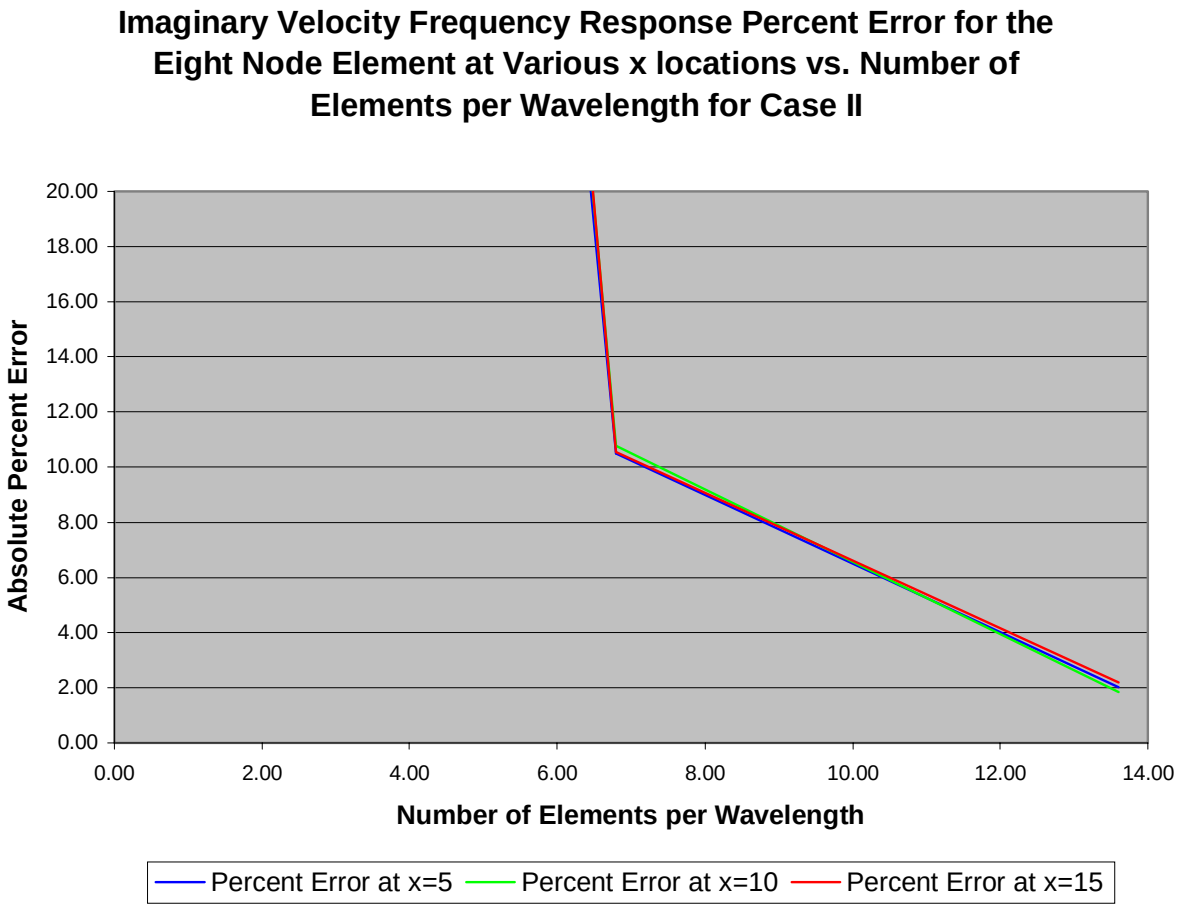

Figure A-14. Imaginary Velocity Frequency Error Response for the Eight Node Element for Case II.

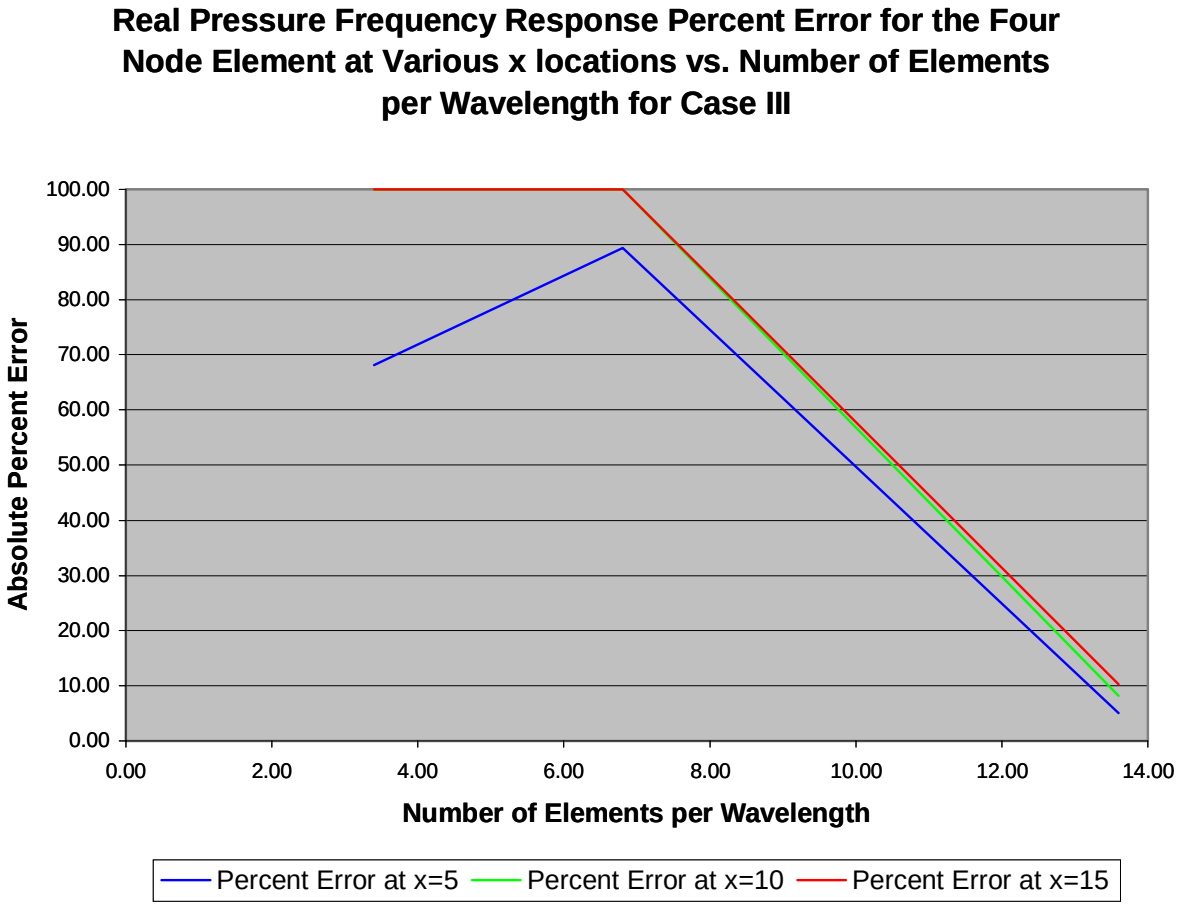

Figure A-15. Real Pressure Frequency Error Response for the Four Node Element for Case III.

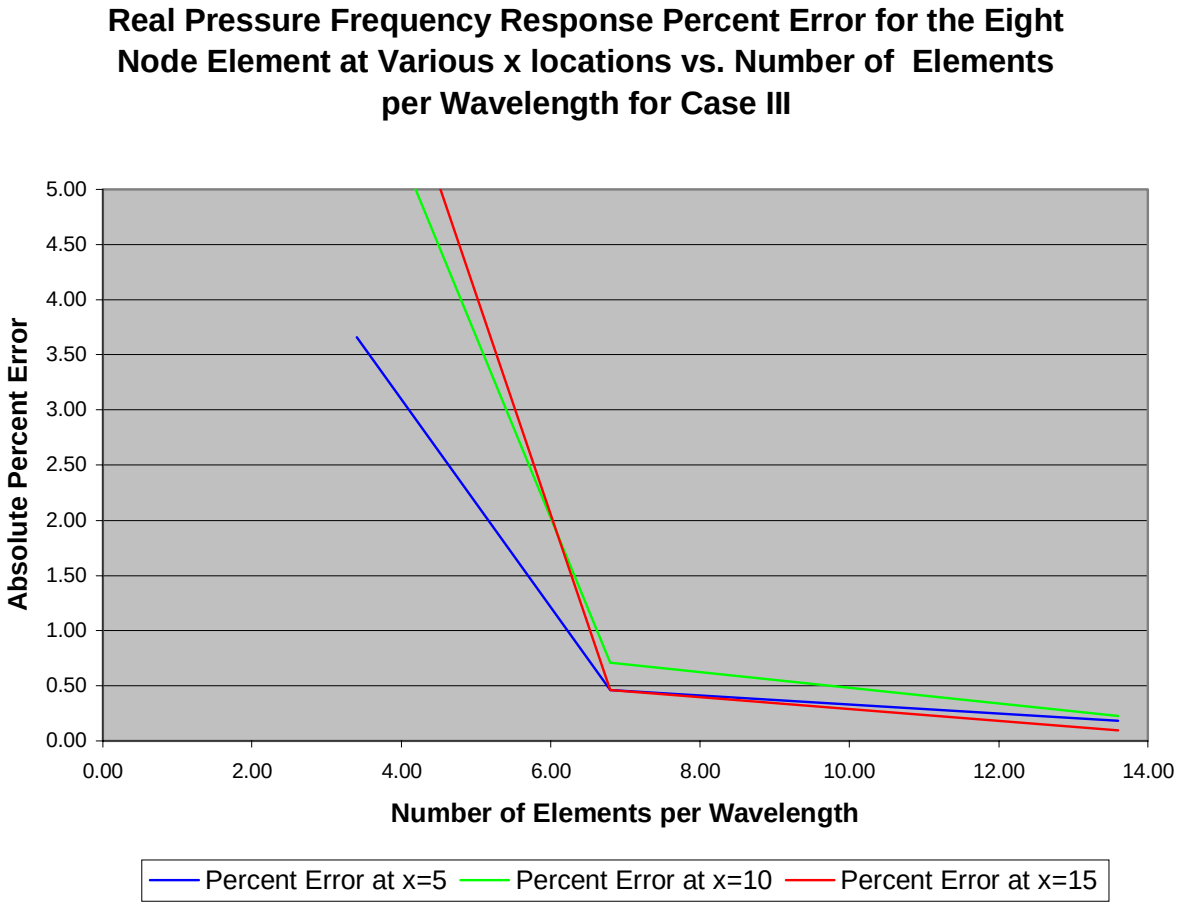

Figure A-16. Real Pressure Frequency Error Response for the Eight Node Element for Case III.

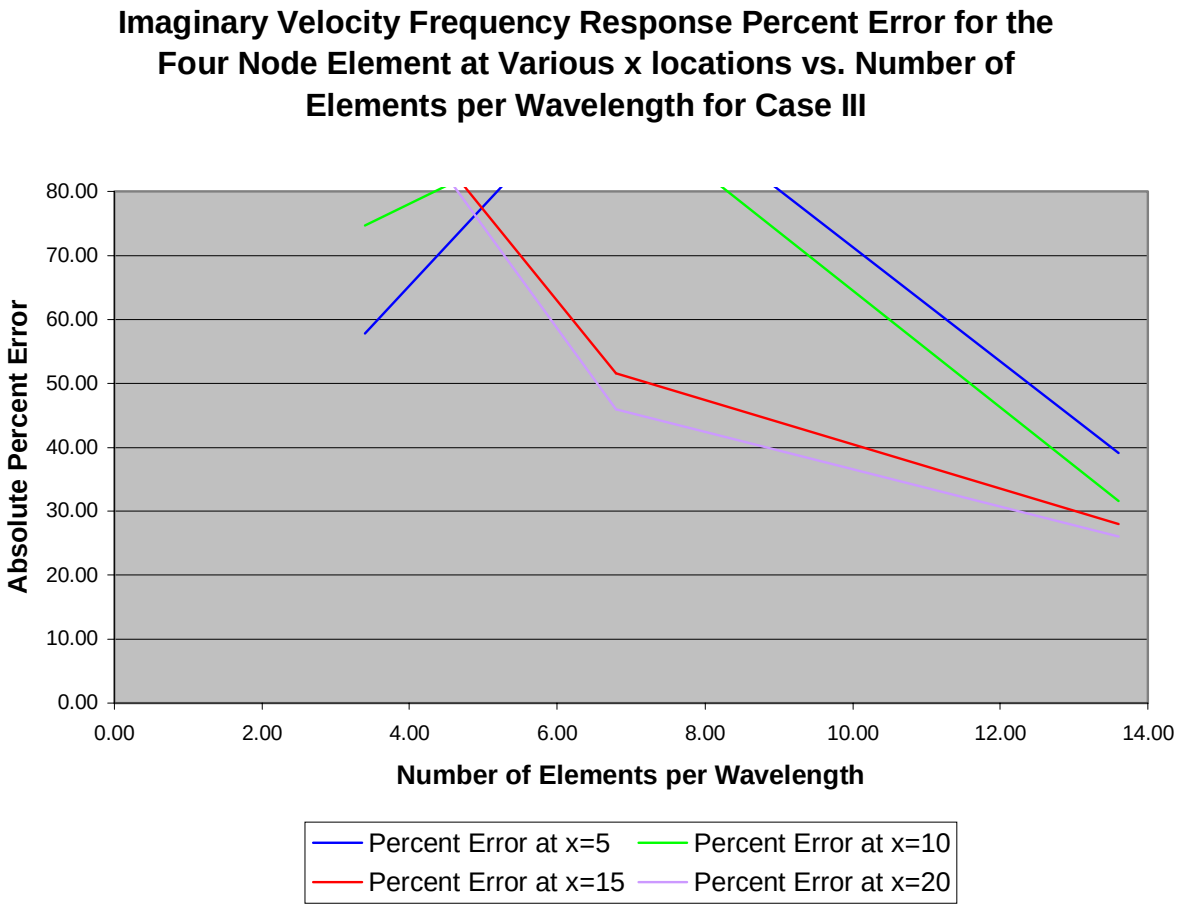

Figure A-17. Imaginary Velocity Frequency Error Response for the Four Node Element for Case III.

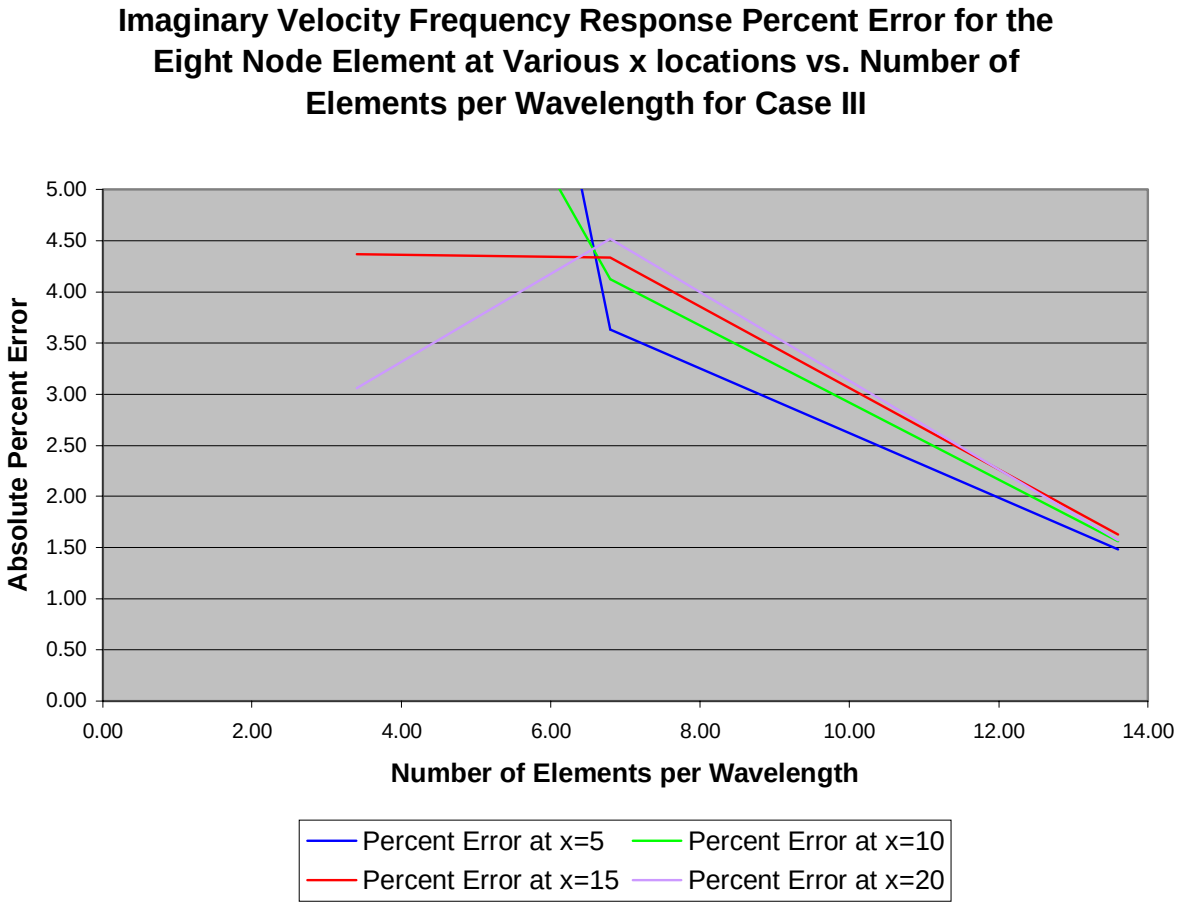

Figure A-18. Imaginary Velocity Frequency Error Response for the Eight Node Element for Case III.

Appendix B[*]

Finite Element Distortion Analysis Figures

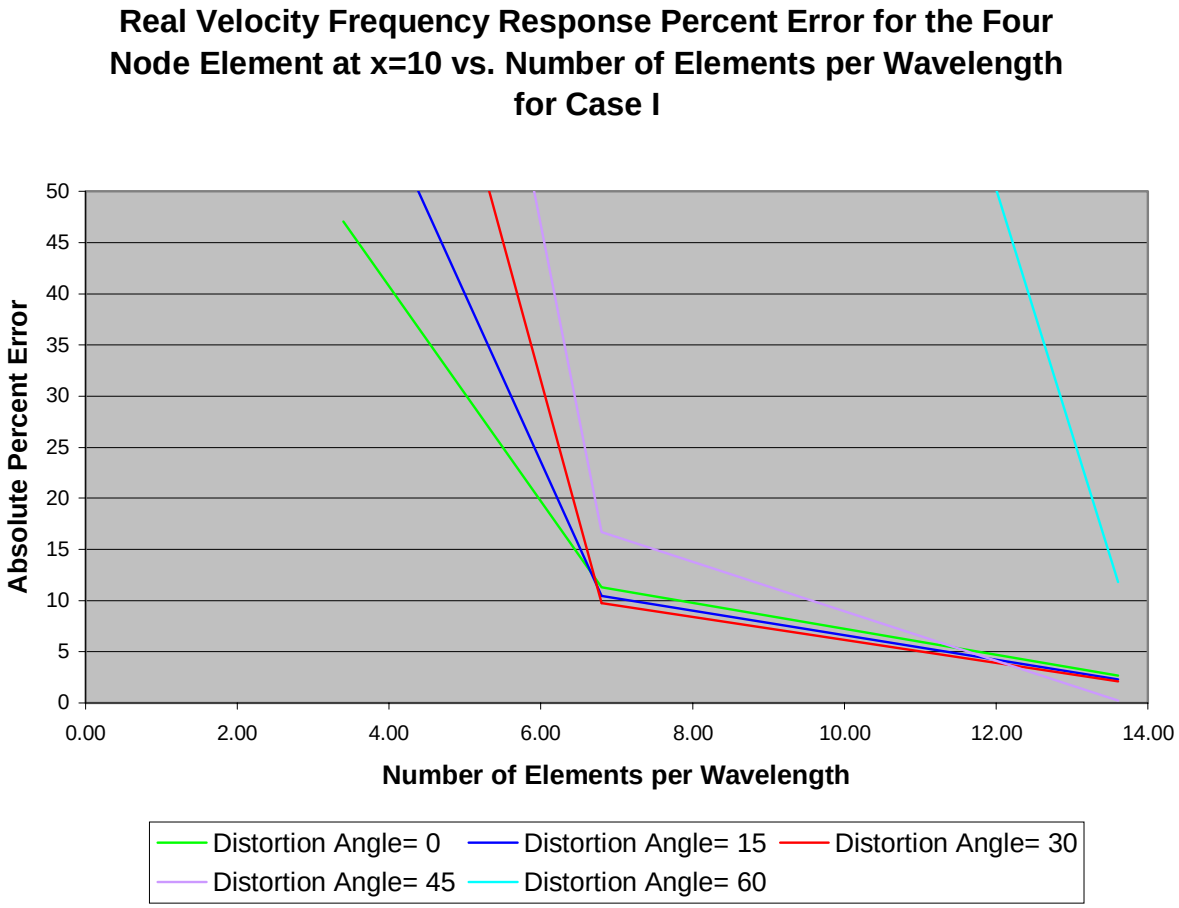

Figure B-19. Real Velocity Frequency Error Response for the Four Node Element for Case I.

[*] The figure numbers in these appendices match the figure number in the text.

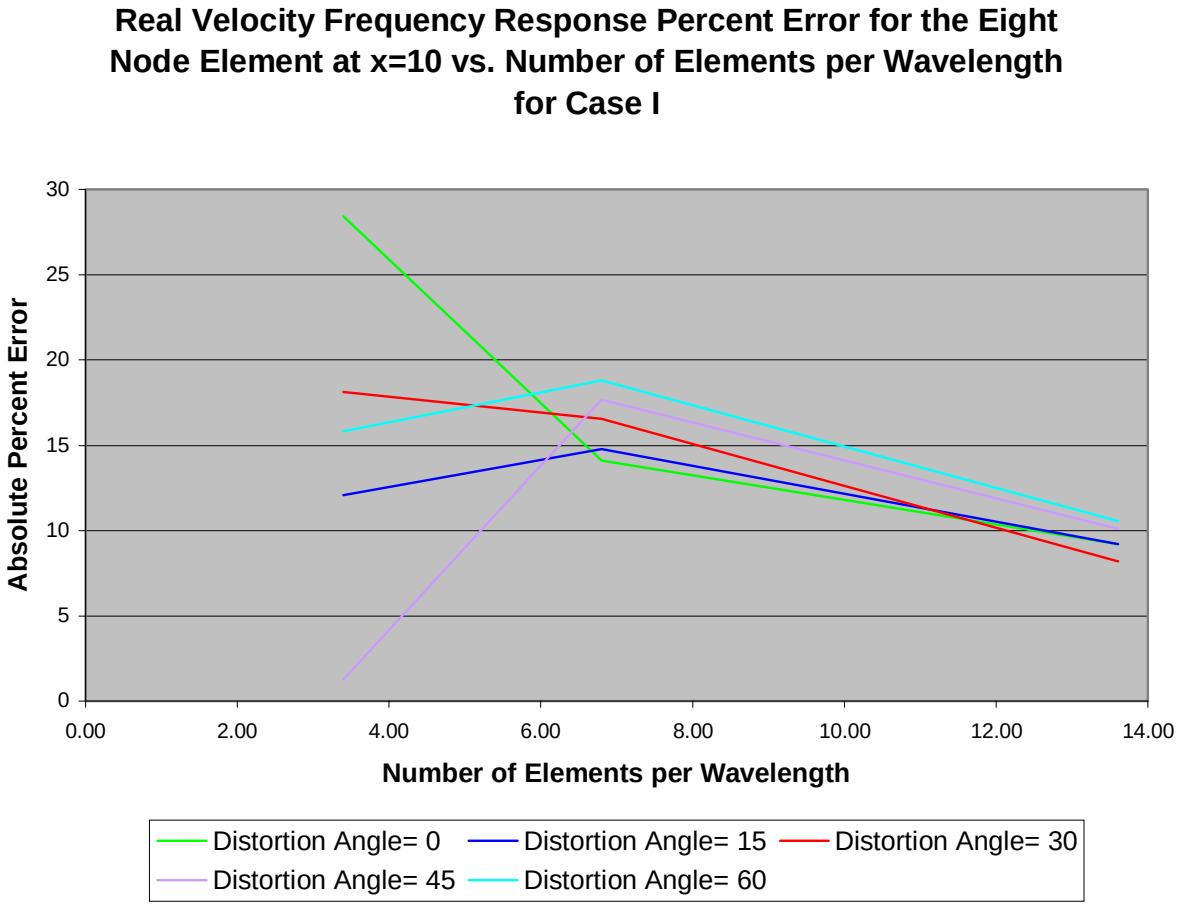

Figure B-20. Real Velocity Frequency Error Response for the Eight Node Element for Case I.

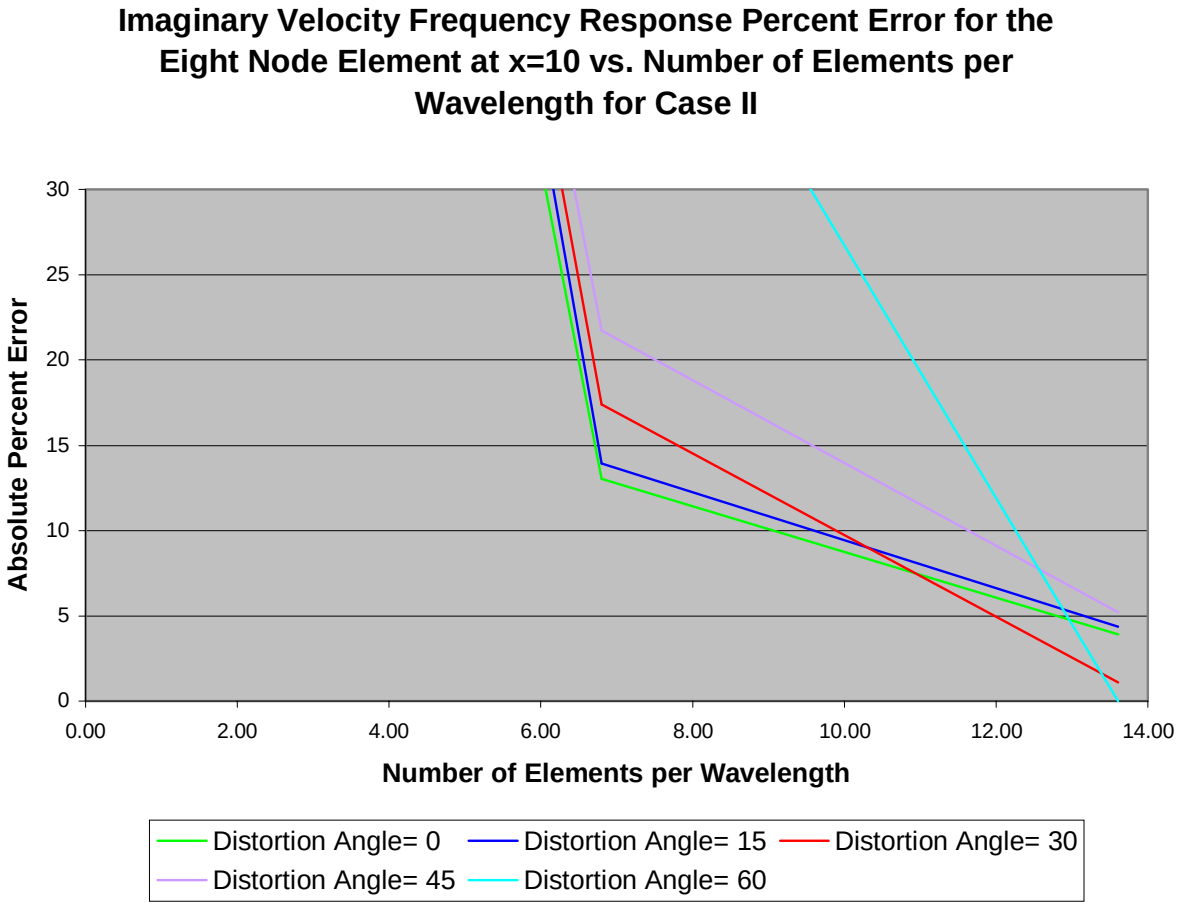

Figure B-21. Imaginary Velocity Frequency Error Response for the Eight Node Element for Case II.

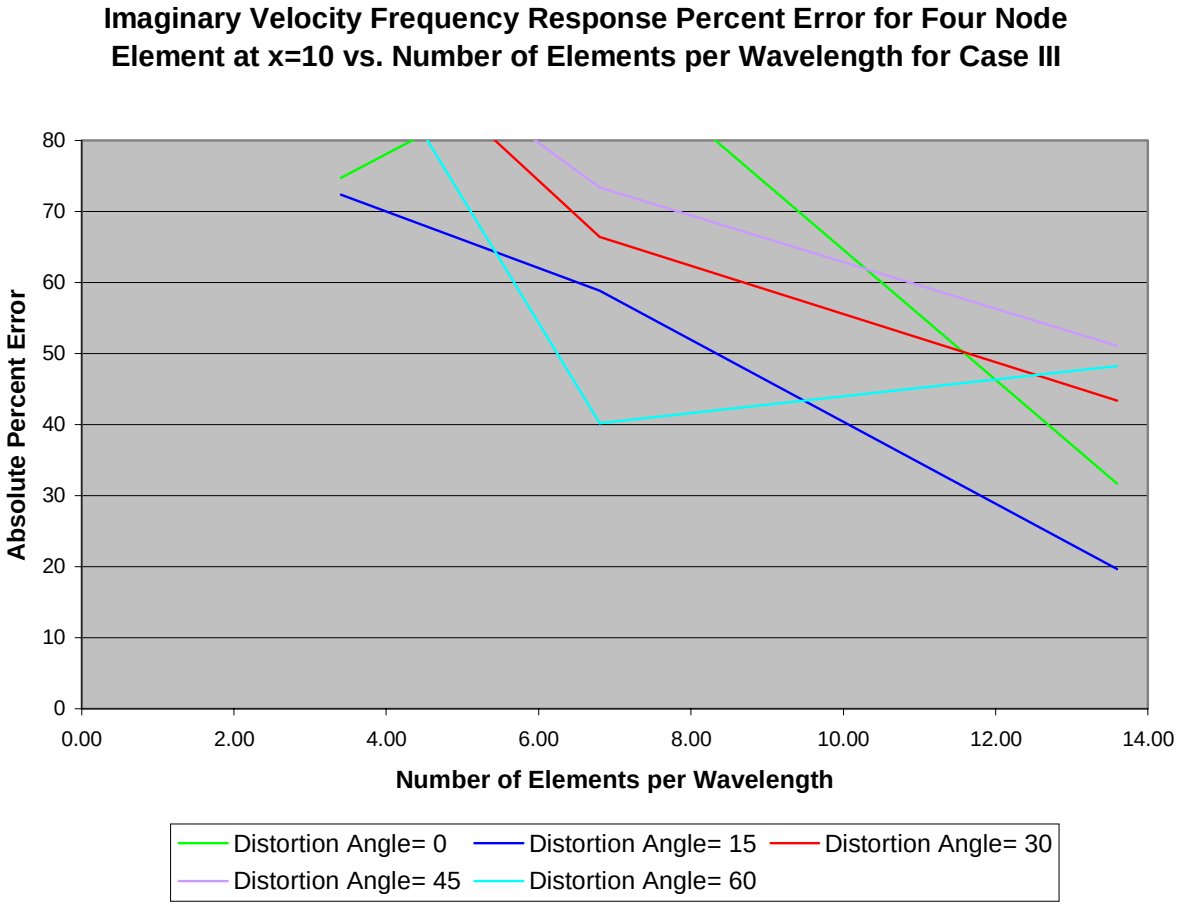

Figure B-22. Imaginary Velocity Frequency Error Response for the Four Node Element for Case III.

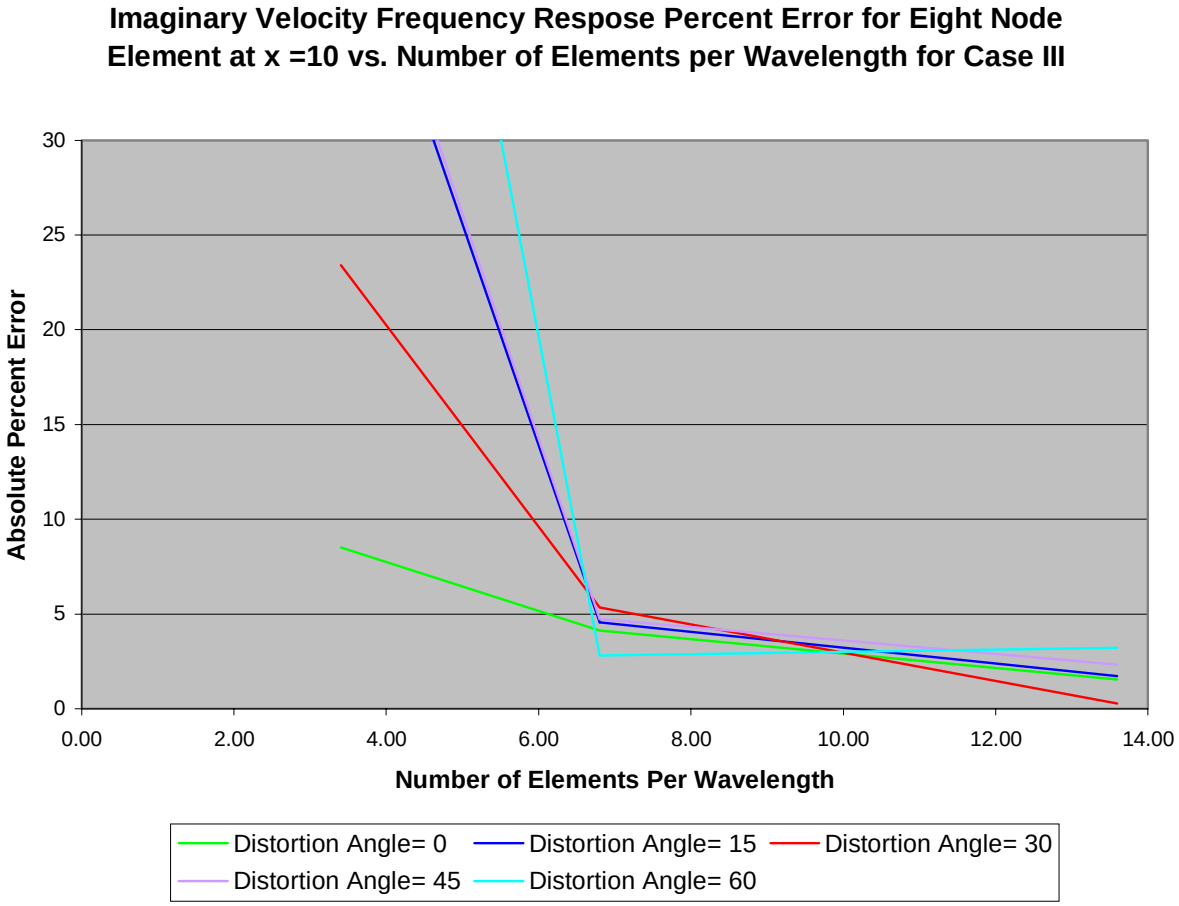

Figure B-23. Imaginary Velocity Frequency Error Response for the Eight Node Element for Case III.

References

1. I.Tag and E. Lumsdaine, “An Efficient Finite Element Technique for Sound Propagation in Axisymmetric Hard Wall Ducts Carrying High Subsonic Mach Number Flows,” AIAA Paper, 1978, 78-1154.

2. R.J. Astley and W. Eversman, “A Finite Element Method for Transmission in Non-uniform Ducts without Flow: Comparison with the Method of Weighted Residuals,” Journal of Sound and Vibration, Vol. 57, No. 3, 1978, pp. 367-388.

3. I. Danda Roy and W. Eversman, “Improved Finite Element Modeling of the Turbofan Engine Inlet Radiation Problem,” Journal of Vibration and Acoustics, Vol. 117, No. 1, 1995, pp. 109-115.

4. P.A.A. Laura et al (3), “Experiments on the Solution of the Helmholtz Equation Using the Finite Element Method and a Variational Approach in the case of Domains of Complicated Boundary Shape,” Journal of Applied Acoustics, Vol. 14, No. 1, 1981, pp. 27-32.

5. C.A Felippa and J.A. DeRuntz, “Acoustic Fluid Volume Modeling by Displacement Potential Formulation, with Emphasis on the Wedge Element,” Computers & Structures, Vol. 41, No. 4, 1991, pp. 669-686.

6. L. E. Kinsler et al (3), Fundamentals of Acoustics. New York: John Wiley & Sons, 1982.

7. R.C. Batra, “An Introduction to the Finite Element Method,” Department of Engineering Science & Mechanics, Virginia Polytechnic Institute & State University, 1995.

8. R. D. Cook, Finite Element Modeling for Stress Analysis. New York: John Wiley & Sons, 1995

Vita

Juan Fernando Betts was born on May 8 1974 in Porto Alegre, Brazil. He graduated magna cum laude with a Bachelors of Science degree from the George Washington University. At George Washington he was involved in a joint project between the Mechanical Engineering Department and the Medical School developing finite element models of the clipping process of cerebral aneurysms.

He has worked as an engineer for ANSER Research Institute preparing technical briefings on U.S. & foreign space vehicles for the Air Force. He has also worked as a junior engineer for Mantech Systems Engineering Corporation developing and analyzing test plans for the Navy AEGIS Defense System.

Juan Fernando Betts came to Virginia Tech in the fall of 96 to pursue his masters' of science degree and has since worked in this finite element and boundary element study in plane wave acoustic in ducts.